European Journal of
Mineralogy
Open Access

Corundum-bearing and spinel-bearing symplectites in ultrahigh-pressure eclogites record high-temperature overprint and partial melting during slab exhumation

Pan Tang[1] and Shun Guo[2,3]

[1]School of Construction Management, Jiangsu Vocational Institute
of Architectural Technology, Xuzhou 221116, China
[2]State Key Laboratory of Lithospheric Evolution, Institute of Geology and Geophysics,
Chinese Academy of Sciences, P.O. Box 9825, Beijing 100029, China
[3]Innovation Academy for Earth Science, Chinese Academy of Sciences, Beijing 100029, China

Correspondence: Shun Guo (guoshun@mail.iggcas.ac.cn)

Abstract. Corundum- and spinel-bearing symplectites after muscovite were found in ultrahigh-pressure (UHP) eclogites from the Dabie terrane, China. Three types of symplectites were recognized based on their mineral assemblages: (1) symplectitic intergrowths of corundum + plagioclase + biotite after phengite (CPB), (2) symplectitic intergrowths of spinel + plagioclase + biotite after phengite (SPB), and (3) symplectitic intergrowths of spinel + plagioclase after paragonite (SP). The microtextures and mineral assemblages of the symplectites, in combination with the results of thermodynamic modeling on local regions, indicate that these symplectites formed by the breakdown of phengite and paragonite during the granulite-facies metamorphic overprint (770–850 °C) of the eclogite at pressures of 0.8–0.9 GPa. Dehydration partial melting reactions occurred during the breakdown of muscovite, which leads to the formation of thin plagioclase films (silicate melts) along grain (garnet, rutile, quartz) boundaries. Mass balance calculations indicate that the development of CPB and SPB symplectites after phengite requires the introduction of Al, Ca, Na, and Fe and loss of Si, Mg, and K. However, the formation of SP symplectites after paragonite requires the input of Mg, Ca, and Fe and removal of Si, Al, and Na. By summarizing the occurrence and growth mechanism of corundum- and spinel-bearing symplectites in global UHP terranes, we find that such symplectites can form by both the subsolidus replacement of an Al-rich anhydrous mineral (kyanite) and the dehydration melting of an Al-rich hydrous phase during high-temperature metamorphism. This study reveals that muscovite-bearing eclogites may experience multiple episodes of partial melting during the slab exhumation, not only at the high-pressure (HP) exhumation stage but also at the lower-pressure metamorphic overprinting stage. Kyanite is a reaction product during the HP partial melting, whereas the low-pressure (LP) melting will consume kyanite. We propose that the occurrence of corundum- and spinel-bearing symplectites after muscovite in eclogites is a potential mineralogical indicator of LP melting in exhumed slabs.

1   Introduction

Partial melting of subducted crust is an important petrologic process, which could modify the rheology of the slabs (e.g., Rosenberg and Handy, 2005; Labrousse et al., 2011), produce adakitic and tonalite–trondhjemite–granodiorite (TTG) magmas (e.g., Goss and Kay, 2006; Palin et al., 2016), and trigger element transfer and chemical differentiation at convergent plate margins (e.g., Hermann et al., 2006; Brown et al., 2011; Stepanov et al., 2014; Ferrero et al., 2016; Guo et al., 2022a). Thus, documenting the partial melting of subduction-zone metamorphic rocks is of significant importance for understanding the lithospheric rheology, thermal structure, and process of material cycling between

the shallow and deep regions of the Earth. However, these rocks generally have experienced complex metamorphic evolution histories during subduction–exhumation processes, involving the prograde stage, the HP–UHP (high-pressure and ultrahigh-pressure) peak stage, and multiple stages of retrogression (e.g., Malaspina et al., 2006; Groppo et al., 2015). Thus, it is essential to precisely identify the potential melting events at different stages and determine the mechanisms and P–T (pressure and temperature) conditions of the partial melting reactions.

Numerous studies have reported the occurrence of partial melting of eclogites in global UHP metamorphic belts, such as those in the Dabie–Sulu orogen, the Kazakhstan Kokshetau massif, and the Western Gneiss Region of Norway (Gao et al., 2017, and references therein). The partial melting events of eclogites are identified based on both the microtextural evidence, such as the felsic films and cuspate minerals around eclogitic matrix grain boundaries, the multiphase solid inclusions (MSIs) in eclogite minerals, and the glass-filled pores in refractory minerals (e.g., Holness and Sawyer, 2008; Zeng et al., 2009; Chen et al., 2014; Gao et al., 2017; Wang et al., 2017), and also the outcrop-scale phenomena of melt flow, such as felsic segregations, eclogitic migmatites, and pegmatites veins (e.g., Liebscher et al., 2007; Song et al., 2014; Wang et al., 2014). Investigations on the above textures and migmatites reveal that the partial melting of the eclogites mostly occurs during the initial exhumation stage at HP conditions (1.5–2.0 GPa) (e.g., Liu et al., 2009; Gao et al., 2012; Tang et al., 2021). However, the temperatures may further increase when these eclogites exhumed to the crustal depth (pressure < 1.5 GPa) (e.g., Gordon et al., 2012; Deng et al., 2019; Cao et al., 2021). Whether the partial melting occurs at lower-pressure conditions during slab exhumation is still largely unknown due to a lack of diagnostic petrological records.

Symplectite textures, which were defined as multiphase fine-grained mineral assemblages with microscopic pseudo structures, typically develop where two minerals are not stable together during the decompression of high-grade metamorphic rocks (e.g., Nakamura and Hirajima, 2000; Obata, 2011; White and Powell, 2011; Groppo et al., 2015; Awalt and Whitney, 2018). The symplectites occurring in the eclogites generally show vermicular intergrowth of minerals or radial structure (e.g., Obata, 2011; Groppo et al., 2015) and formed through replacing the eclogite-facies minerals under amphibolite- to granulite-facies conditions (e.g., Godard and Mabit, 1998; Faryad et al., 2006, 2015). Especially, some symplectites may contain minerals that typically form under high-temperature (HT) to ultra-HT (UHT) conditions (e.g., sapphirine, corundum, spinel) (Janák et al., 2012; Faryad et al., 2015; Tual et al., 2017; Tumiati et al., 2018; Cruciani et al., 2019), implying an obvious heating process at decompression. Thus, the symplectite textures in the eclogites, which contain the HT minerals, have a potential to record the LP partial melting process.

In this study, we report distinct corundum- and spinel-bearing symplectites in the UHP eclogites from the Dabie terrane, China. We present comprehensive investigations of petrology, Raman analyses, mass balance calculations, and thermodynamic modeling to constrain the formation mechanism and P–T conditions of these symplectites. Our results reveal that the corundum- and spinel-bearing symplectites formed by the partial melting of phengite and paragonite during the granulite-facies overprinting. This study indicates that the UHP eclogites have experienced multiple episodes (HP vs. LP) of partial melting during exhumation. We also summarize and compare the occurrence, condition, and formation mechanism of corundum- and spinel-bearing symplectites in eclogites from global UHP terranes and stress that the occurrence of such symplectites replacing muscovite in eclogites provides important implications for fluid or melt actions in exhumed slabs. Mineral abbreviations used in the text, figures, and tables are based on Whitney and Evans (2010).

2   Geological background and sample description

The Dabie–Sulu metamorphic terrane, located in the eastern portion of central China collision belt (Fig. 1a), formed by the subduction of the South China Block (SCB) beneath the North China Block (NCB) in the Triassic (e.g., Zhang et al., 2009a). The Dabie terrane is located in the southwestern part of the Dabie–Sulu UHP terrane, which is separated by ∼ 500 km of the sinistral Tan–Lu strike-slip fault. The occurrence of micro-diamond and coesite in metamorphic minerals suggests that the South China Block had been subducted to 120 km depths at least (e.g., Okay et al., 1989; Xu et al., 1992). The Dabie terrane is generally subdivided into six metamorphic zones from north to south (Fig. 1a): (1) the north Huaiyang low-grade metamorphic zone, (2) the north Dabie metamorphic core complex, (3) the coesite eclogite-facies metamorphic zone, (4) the quartz eclogite-facies metamorphic zone, (5) the amphibolite-facies metamorphic zone, and (6) the greenschist- to blueschist-facies metamorphic zone (Zheng et al., 2005). The eclogite-facies metamorphic zones mainly consist of various types of gneisses, which are intruded by numerous Cretaceous granites (Fig. 1a) (Faure et al., 2003; Zhang et al., 2009a). Variable-size blocks of eclogite, garnet peridotite, marble, jadeite quartzite, peridotite, and marble can be found in the gneisses.

Petrological evidence for partial melting of UHP eclogites and gneisses has been increasingly found in the Dabie terrane (e.g., Xia et al., 2008; Gao et al., 2012; Liu et al., 2014; Groppo et al., 2015). The production of silicate melts during the melting can be evidenced by the occurrences of (1) MSIs of Kfs + Pl + Qz ± Ep ± Brt in eclogite minerals (Gao et al., 2012; Liu et al., 2013, 2019; Tang et al., 2021) and (2) diagnostic microstructures among mineral grain boundaries, such as melt-filled pools, feldspar thin films, and melanosome
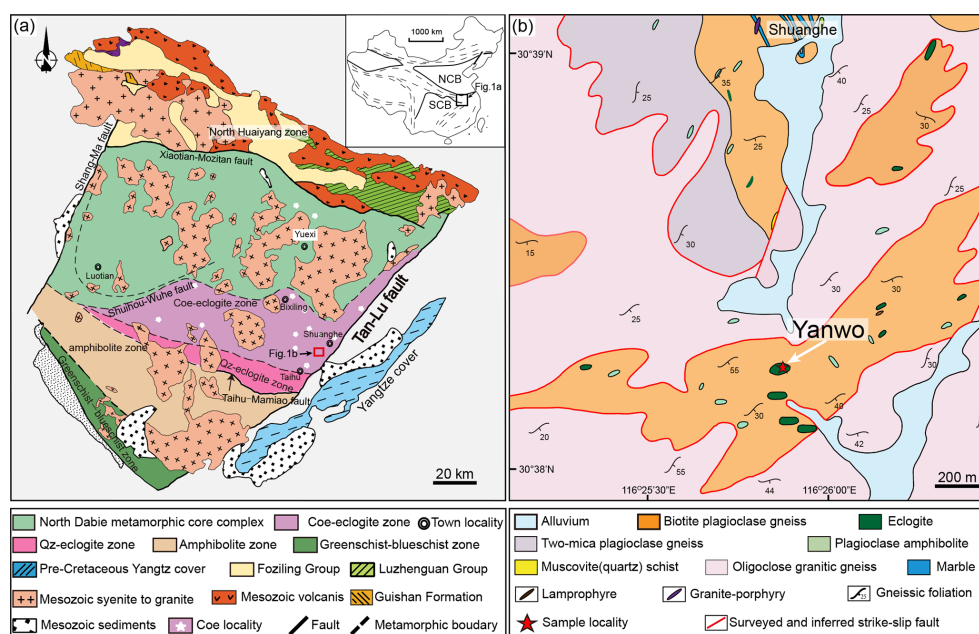
Figure 1. (a) Regional geological map of the Dabie terrane in eastern China. **(b)** Sketch of the lithologic distribution and sample locality (the star) in the Yanwo area.

patches/layers (Xia et al., 2008; Deng et al., 2019; Liu et al., 2019). Petrologic and experimental modeling indicates that the partial melting occurs during the eclogite-facies stage, mostly by dehydration-driven or fluid-fluxed melting of muscovite (Liu et al., 2009, 2013; Gao et al., 2012; Tang et al., 2021).

The present study area is located in the Yanwo area in the Dabie UHP terrane (Fig. 1b), where UHP eclogites occur as various sizes of lenses and blocks (a few centimeters to over hundreds of meters in length) within granitic gneisses (Fig. 1b). A new petrological study (Tang et al., 2021) indicated that the Yanwo UHP eclogites had experienced a clockwise P–T metamorphic path with peak metamorphic conditions of 2.8–3.1 GPa and 630–700 °C. Moreover, both metamorphic dehydration (~ 2.2–2.7 GPa and 620–750 °C) and partial melting events (~ 1.5–2.0 GPa and 700–750 °C) during exhumation were recognized in the Yanwo eclogites and HP veins (Tang et al., 2021).

In this study, two representative retrograded UHP eclogites, 17YW3 and 17YW7 (Fig. 2a), which develop abundant corundum-bearing and spinel-bearing symplectites after muscovite, were investigated. The two eclogites exhibit a similar petrological texture and have a similar mineral assemblage. They consist of garnet (25 vol %–30 vol %), omphacite (20 vol %–25 vol %), epidote (15 vol %–20 vol %), amphibole (~ 15 vol %), phengite (2 vol %–6 vol %), paragonite (~ 3 vol %), quartz (~ 3 vol %), and various amounts of accessory rutile and apatite (Fig. 2b). Garnet shows euhedral to subhedral shapes with a size of 0.5–1 mm and contains inclusions of omphacite, rutile, quartz, and zircon

(Fig. 2c, d). Omphacite occurs as both matrix minerals and inclusions in garnet, which is partially replaced by fine-grained symplectites of clinopyroxene (diopside) + plagioclase $\pm$ orthopyroxene (Figs. 2e, f, and 3a). Clinopyroxene in the symplectites exhibits a rodlike shape, and orthopyroxene shows a platy shape. Epidote occurs as the subhedral porphyroblasts (Fig. 2c, d). Fine-grained hematite occasionally occurred (Figs. 2e, f, and 3b). Muscovite (phengite and paragonite) occurs as subhedral flakes (0.5–1.5 mm) and was partially replaced by symplectites of corundum- and spinel-bearing assemblages.

3   Analytical methods

Backscattered electron (BSE) images were acquired using the Nova Nano scanning electron microscope (SEM) 450 at the Institute of Geology and Geophysics, Chinese Academy of Sciences (IGGCAS). The operation conditions are as follows: accelerating voltage of 15 kV, a beam current of 6 nA, and working distance of 6 mm.
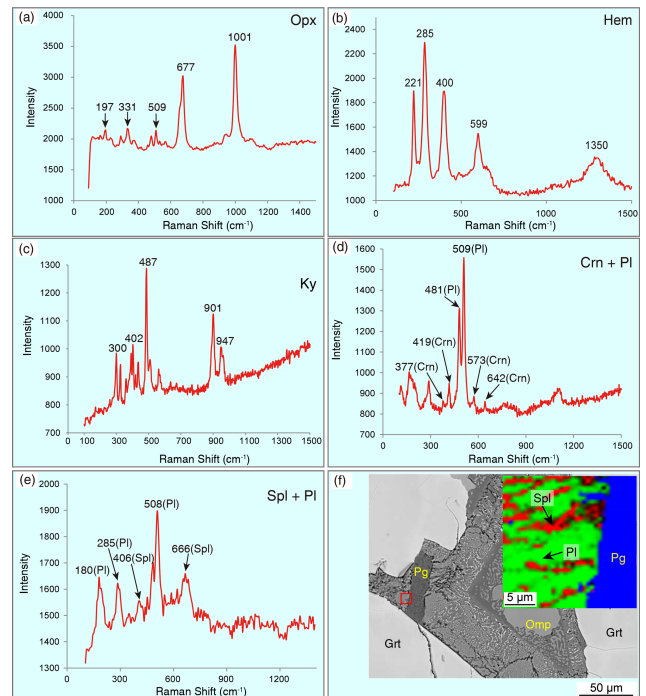
Fine-grained minerals (< 1 µm) in symplectite assemblages were identified using a WITec alpha 300R confocal Raman microscope with a 532 nm excitation laser at the IGGCAS. The detail positions of peaks in Raman spectra, referring to the RRuff online database (https://rruff.info/, last access: 15 June 2023), are as follows: 377, 419, 573, and 642 cm^{-1} for corundum; 406 and 666 cm^{-1} for spinel; 402, 487, 901, and 947 cm^{-1} for kyanite; 197, 331, 509, 677, and 1001 cm^{-1} for orthopyroxene; 180, 285, 481, and 508 cm^{-1} for plagioclase; and 221, 285, 400, 599, and 1350 cm^{-1} for
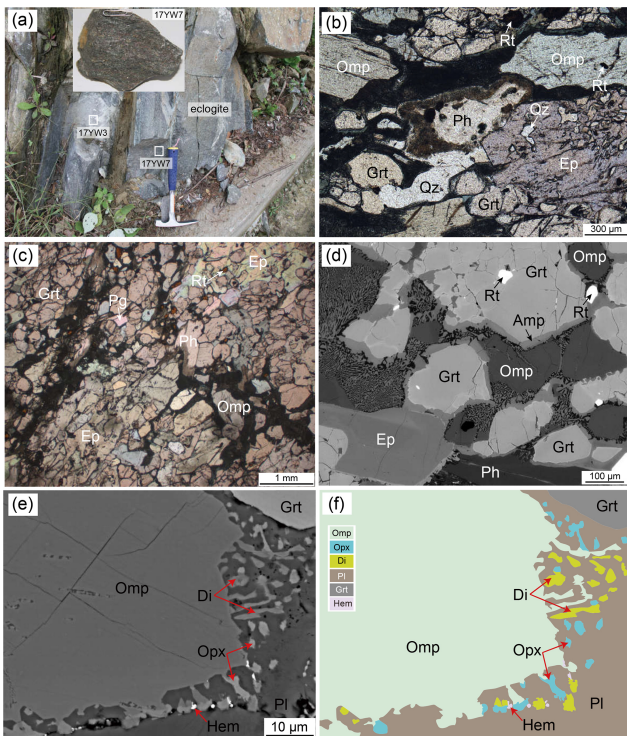
Figure 2. Field outcrop **(a)**, hand specimen **(b)**, and photomicrographs **(c, d)** of the studied eclogites. White boxes in **(a)** showing the sampling locations in this study. BSE image **(e)** and its sketch map **(f)** showing the Di + Opx + Pl symplectites after omphacite in the eclogites.

Figure 3. (a–e) The Raman spectrum of minerals in symplectites from the eclogites 17YW3 and 17YW7. **(f)** BSE image showing the Spl + Pl symplectites (SP) after paragonite. The inset shows the Raman map of the red box in **(f)**.

hematite. For single spectrum analyses, the integration time and accumulations are set as 10 and 2 s, respectively. The size of the laser spot was 0.4 µm, and the laser power was 2–10 mW. Raman mapping was set at the step of 0.3–0.5 µm with an acquisition time of 3–5 s and one accumulation. The accuracy of Raman line shifts was checked by regular measurements of the 521 cm^{-1} signal for a synthetic monocrystalline Si standard.

Compositions of minerals were analyzed using a CAMECA SXFive electron probe microanalyzer (EPMA) at the IGGCAS. The accelerating voltage was 20 kV, and the beam current was 100 nA for fine-grained minerals (orthopyroxene, corundum, spinel, and kyanite) with a 1 µm beam diameter. The operating conditions for other minerals (plagioclase, muscovite, biotite, garnet, clinopyroxene, and amphibole) were 15 kV accelerating voltage, 18 nA beam current, and 5 µm beam diameter. The natural minerals and synthetic oxides used for calibration are diopside (Si, Ca, and Mg), albite (Na), orthoclase (K), rutile (Ti), Al_2O_3 (Al), FeS_2 (Fe), Cr_2O_3 (Cr), MnO (Mn), ZnS (Zn), and NiO (Ni). A program based on the ZAF procedure was used for data corrections of minerals (Armstrong, 1995). The analytical uncertainties for most major elements are less than 2 % relative.

The X-ray maps (Si, Al, Fe, Ca, Mg, Na, and K) of the symplectite regions were acquired by wavelength dispersive spectroscopy (WDS) analyses using the CAMECA SXFive EMPA at the IGGCAS. The operation conditions were 15 kV accelerating voltage, 150 nA beam current, and a dwell time per point of 45 ms. The X-ray maps were produced at a 1024 × 1024 resolution.

4   Results

4.1   Petrography

Three types of symplectites after muscovite (phengite and paragonite) were recognized according to the mineral assemblages (Figs. 4–6) in the studied eclogites.
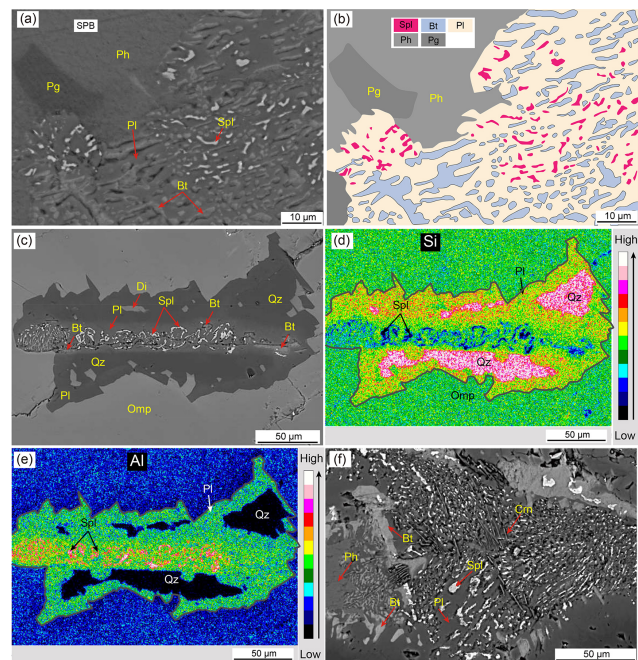
The first type of symplectite is the intergrowth assemblages of corundum + plagioclase + biotite after phengite (CPB). Figure 4 shows a typical CPB assemblage with 10 vol %–20 vol % of corundum, 55 vol %–65 vol % plagioclase, and 20 vol %–25 vol % of biotite (Fig. 4a–c, h–k). The corundum occurs as needlelike crystals ranging from 5 to 100 µm in length and has an intergrowth direction the same as the matrix of plagioclase (Fig. 4c–g). The biotite typically shows a tabular shape (Fig. 4c–k). Anhedral kyanite is occasionally found near the CPB symplectite, and the crystal size of kyanite is much bigger than the symplectitic minerals
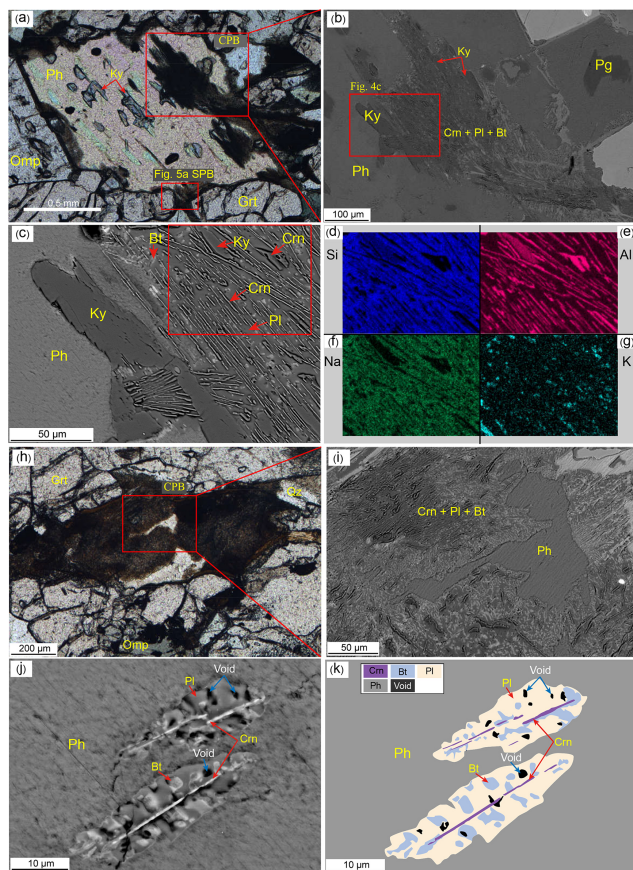
Figure 4. Photomicrographs (**a, h**), and BSE images (**b, c, i, j**) showing the Crn + Pl + Bt symplectites (CPB) after phengite. (**d–g**) X-ray maps of the selected red box in (**c**). (**d**) X-ray map of Si. (**e**) X-ray map of Al. (**f**) X-ray map of Na. (**g**) X-ray map of K. (**k**) Sketch map of (**j**).

Figure 5. BSE images (**a, c**) and sketch map (**b**) showing the Spl + Pl + Bt symplectites (SPB) after phengite. (**d**) X-ray map of Si of (**c**). (**e**) X-ray map of Al of (**c**). (**f**) BSE image showing the SPB symplectite intergrown with the CPB symplectite in eclogite 17YW7.

(Fig. 4a–c). The CPB symplectites not only distribute around the phengite but also develop in the interior regions of the phengite where small fractures develop (Fig. 4j, k). Moreover, the CPB symplectites in the phengite display an internal porosity with sizes of irregular voids down to a few tens of nanometers (Fig. 4j, k).

The second type of symplectite is the intergrowth assemblages of spinel (15 vol %–20 vol %) + plagioclase (60 vol %–65 vol %) + biotite (15 vol %–20 vol %) after phengite (SPB). The minerals in the SPB symplectite typically show subhedral to anhedral shapes. Spinel is generally vermicular with a size of 1–5 μm in the matrix of plagioclase (Fig. 5a–c). The growth of spinel is perpendicular to the phengite. Biotite forms tabular and subhedral crystal and has its long axes parallel or subparallel to the orientation of spinel. Several quartz grains appear in the symplectite surroundings (Fig. 5d, e). However, the spinel grains are never found to be in direct contact with quartz. Rather, spinel is separated from quartz by plagioclase. Kyanite is not observed in the SPB symplectites. In addition, we find that a single

phengite grain can be replaced by both CPB and SPB symplectites (Fig. 4a). Both types of symplectites coexist with each other (Fig. 5f).

The third type of symplectite is the intergrowth assemblages of spinel + plagioclase after paragonite (SP). Figure 6a shows a typical SP symplectite, which is consisted of 25 vol %–35 vol % spinel and 60 vol %–70 vol % plagioclase. This type of symplectite develops after both matrix paragonite (Fig. 6a, b) and paragonite inclusions in omphacite (Fig. 6c, d). Amphibole occasionally occurs in the SP symplectites (Fig. 6c). The Raman mapping (Fig. 3f), BSE images (Fig. 6b, d), and X-ray maps (Fig. 7) show that the spinel grows perpendicularly to the paragonite. The grain size of spinel (up to 20 μm) in the SP symplectites after paragonite is relatively larger compared to that in SPB symplectites after phengite. Omphacite in contact with the SP symplectites shows a compositional variation (Fig. 6a, c). In addition, the orthopyroxene (Opx) grains after omphacite are found to occur adjacent to the SP symplectite (Fig. 6d).

Interestingly, a distinct texture of plagioclase films was found near the three types of symplectites (Fig. 8). In the CPB (Fig. 8a–d), SPB (Fig. 8e, f), and SP (Fig. 8g) symplectite domains, many fine films of plagioclase can be observed to distribute along the boundaries of the symplectites and other minerals (e.g., Qz and Rt). The films show finely tapered ends, suggesting consistently small dihedral angles (Fig. 8b, d, e, g). In the symplectite domain, plagioclase with
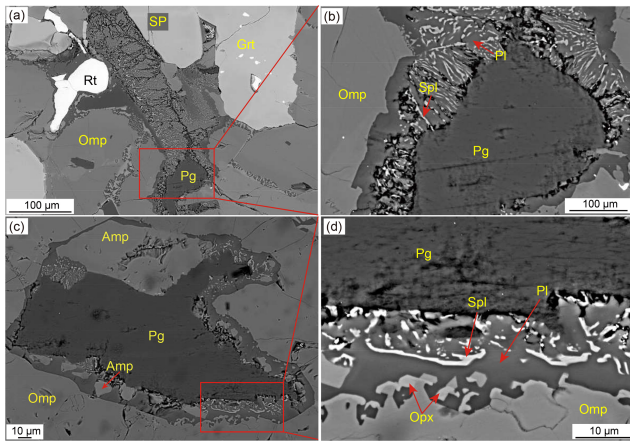
Figure 6. BSE images showing the SP symplectites after paragonite in eclogite 17YW3 **(a, b)** and 17YW7 **(c, d)**. **(a)** The symplectitic intergrowths of spinel + plagioclase after matrix paragonite. **(b)** An enlarged view of part of the symplectite in **(a)** showing that spinel grows perpendicularly to the matrix paragonite. **(c)** The symplectitic intergrowths of spinel + plagioclase + amphibole after paragonite inclusions. **(d)** An enlarged view of part of the symplectite in **(c)** showing that Opx grains after omphacite occurs adjacent to the SP symplectite.

clear cuspate margins extends along the symplectite boundaries, and the surrounding mineral grains develop an embayed shape (Fig. 8e–g). Locally, the plagioclase, intergrown with biotite, occurs at the junction between garnet grains and forms the films separating these garnet grains (Fig. 8h).

4.2   Mineral chemistry

Most of symplectitic minerals have a very small grain size. In this study, the minerals whose grain sizes are larger than 1 µm were analyzed due to instrument limitation. Representative compositions of minerals are listed in Tables 1 and 2 and Tables S1–S3 in the Supplement.

4.2.1   Corundum and spinel

The needle corundum in the CPB symplectite is almost pure Al_2O_3 (> 99 wt %) with a minor amount of FeO (0.52–1.01 wt %) (Table 1).

Spinel in both the SPB and SP symplectites is present as a solid solution between hercynite ($FeAl_2O_4$) and Mg-spinel ($MgAl_2O_4$) (Fig. 9a). The spinel has X_{Mg} ($= Mg/(Mg + Fe^{2+})$) of 0.38–0.42 and minor amounts of Cr_2O_3 (≤ 0.12 wt %), ZnO (≤ 0.32 wt %), and MnO (≤ 0.13 wt %).

4.2.2   Plagioclase

Plagioclase shows an obvious compositional difference (Table 2, Fig. 9b). The plagioclase in the CPB, SPB, and SP symplectites has albite components of 59 mol %–74 mol % and anorthite components of 22 mol %–39 mol %. The pla-

gioclase intergrown with diopside and orthopyroxene after omphacite has higher albite (87 mol %–92 mol %) and lower anorthite (8 mol %–13 mol %) components than that after muscovite. The plagioclase in the films has a similar composition with the symplectitic plagioclase after muscovite.

4.2.3   Muscovite and biotite

Phengite in the eclogites has high Si contents (3.34–3.45 pfu) and X_{Mg} values of 0.65–0.89. Paragonite has relatively low Si contents (3.01–3.04 pfu), high Na contents (0.84–0.91 pfu), and high K contents (0.05–0.07 pfu) (Table S1). Biotite in the CPB and SPB symplectites has X_{Mg} values of 0.61–0.66 and Ti contents of 0.03–0.19 pfu (Table S1).

4.2.4   Garnet

The matrix garnet is dominantly composed of almandine (45 mol %–51 mol %), pyrope (25 mol %–35 mol %), grossular (17 mol %–25 mol %), and small amounts of spessartine (≤ 1 mol %) (Table S2). The compositional profile of garnet shows an increase in grossular content and decreases in pyrope and almandine contents from the cores to rims at nearly constant spessartine content (Fig. 9c, d).

4.2.5   Clinopyroxene

The omphacite in the eclogites has 30 mol %–45 mol % jadeite, 38 mol %–47 mol % diopside, 6 mol %–19 mol % aegirine, and 2 mol %–9 mol % hedenbergite contents (Table S3). The omphacite in contact with paragonite has lower Mg, Ca, and Fe compositions than that far from the paragonite (Fig. 9e, f). The clinopyroxene in symplectites after omphacite has diopside contents of 56 mol %–60 mol %, hedenbergite contents of 28 mol %–37 mol %, jadeite contents of 3 mol %–12 mol %, and aegirine contents of 1 mol %–6 mol %.

4.2.6   Orthopyroxene

Rare orthopyroxene occurs as retrograde fine-grained corona after omphacite. Orthopyroxene has X_{Mg} values of 0.67–0.76 with low Al_2O_3 contents (< 3.3 wt %) and CaO contents of 0.19 wt %–1.16 wt % (Table S3, Fig. 9g).

4.2.7   Amphibole and kyanite

The matrix amphibole is classified as edenite according to Leake et al. (1997) with X_{Mg} of 0.68–0.75 and $(Na + K)^A$ of 0.72–0.88. The amphibole in the SP symplectites is classified as pargasite or magnesiokatophorite with X_{Mg} of 0.70–0.75 and $(Na + K)^A$ of 0.65–0.97 (Table S4). Kyanite is almost a pure Al_2SiO_5 endmember with minor FeO contents (< 0.73 wt %).
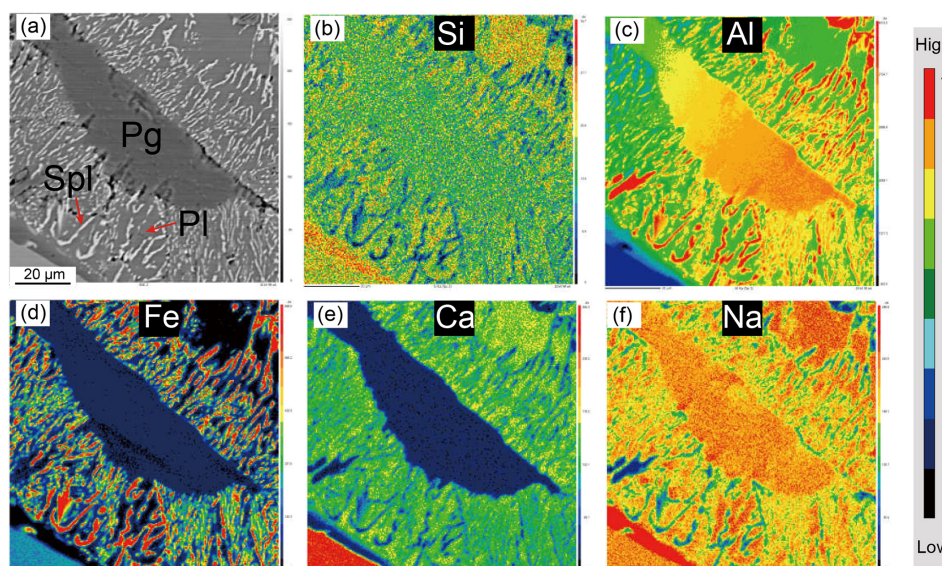
Figure 7. BSE image **(a)** and X-ray maps **(b–f)** of Si, Al, Fe, Ca, and Na of the SP symplectite after paragonite. **(b)** X-ray map of Si. **(c)** X-ray map of Al. **(d)** X-ray map of Fe. **(e)** X-ray map of Ca. **(f)** X-ray map of Na.

5 Discussion

5.1 Petrological interpretation of symplectites

The first type of symplectite (CPB) typically develops at the external boundary of coarse-grained phengite or occurs along the internal fractures of phengite (Fig. 4b, c). The mineral assemblages are generally distributed aligning parallel or subparallel to the long axis of the original phengite. This orientation relationship is consistent with the topotactic nucleation of the reaction products within the dehydroxylated phengite lattice (e.g., Brearley and Rubie, 1990; Rodriguez-Navarro et al., 2003; Devineau et al., 2006). Experimental investigations have shown that the thermal decomposition of phengite at high-T ($\geq 750\,°C$) and low-P ($< 1.0\,GPa$) conditions could generate Al-rich oxides as a peritectic phase with characteristic dendritic to skeletal morphologies (e.g., Brearley and Rubie, 1990; Devineau et al., 2006; Masotta et al., 2018), which is consistent with the textures of the skeletal and needle corundum crystals in the CPB symplectites. Similar textures have been also reported in phengite-bearing eclogites from the Black Forest, Germany, and were interpreted as the products of phengite melting by the reaction Ph $\rightarrow$ Crn + Pl + Bt + other Al silicates + melt during the transformation from a granulite-facies to a HT–LP amphibolite-facies stage (Wimmenauer and Stenger, 1989). Moreover, based on the petrological observation and P–T estimation, Dokukina et al. (2017, 2021) revealed the polymineral assemblages consisting of Crn + Kfs + Bt + newly formed Ms + dumortierite in phengite-bearing quartz-feldspar rocks from the Belomorian eclogite province (Russia) as a dehydration melting product of phengite by the reaction Ph $\rightarrow$

Crn + Kfs + Bt + melt under HT granulite-facies conditions. Furthermore, the compositions of corundum in CPB symplectites from the studied eclogites (0.52 wt %–1.01 wt % for FeO) are similar to those of the corundum ($< 2.70\,wt\,\%$ for FeO) produced by the experimental melting of phengite (e.g., Brearley and Rubie, 1990; Rodriguez-Navarro et al., 2003; Devineau et al., 2006; Masotta et al., 2018). We thus consider that the corundum (Crn)-bearing symplectites in the Dabie eclogites are not formed by the subsolidus reactions of phengite. Rather, they are most likely the partial melting products of phengite. The anhedral shape and serrated grain boundary of the residual phengite (Fig. 4a) are also consistent with those produced by the partial melting of phengite (Lang and Gilotti, 2007).

Interestingly, kyanite was found to always coexist with the CPB symplectites (Fig. 4b, c) but is never found near the other two types of symplectites, indicating that kyanite is also involved in the reaction of CPB symplectite formation. The grains of kyanite are much coarser than those of the symplectite minerals (Fig. 4c), suggesting that the kyanite is a reactant rather than a product of reaction. The interpretation is supported by many previous studies (e.g., Nakamura and Hirajima, 2000; Janák et al., 2012; Moulas et al., 2015), which reveal that kyanite could be replaced by the symplectites of Crn + Pl during HT metamorphism ($\geq 700\,°C$). Thus, we conclude that the reaction responsible for the CPB symplectite formation is as follows: Ph + Ky $\rightarrow$ Crn + Pl + Bt + melt.

The second type of symplectite (SPB) also formed by the consumption of phengite (Fig. 5a, b). Vermicular spinel, rather than acicular corundum, occurs in the SPB symplectites. Several experimental studies reveal that phengite can

Table 1. The representative major element compositions of corundum and spinel in Yanwo eclogites (oxide concentrations in wt %).

Mineral	Crn			Spl					
texture	In symplectites of CPB			In symplectites of SPB			In symplectites of SP		
SiO_2	0.42	0.18	0.09	0.55	1.26	0.29	1.15	0.55	1.24
TiO_2	0.28	0.02	0.02	0.02	0.20	0.00	0.43	0.02	0.01
Al_2O_3	98.72	98.91	98.78	62.25	60.80	62.32	60.80	62.26	60.97
Cr_2O_3	0.18	0.19	0.28	0.07	0.02	0.07	0.12	0.07	0.00
FeO	0.89	0.52	0.56	26.39	26.06	26.36	26.79	26.39	26.42
MnO	0.01	0.00	0.01	0.08	0.12	0.08	0.10	0.08	0.10
MgO	0.03	0.00	0.00	10.56	10.07	10.55	9.05	10.67	10.23
CaO	0.12	0.04	0.04	0.14	0.37	0.17	0.35	0.14	0.44
Na_2O	0.14	0.03	0.02	bdl[a]	bdl	bdl	bdl	bdl	bdl
K_2O	0.01	0.01	0.01	bdl	bdl	bdl	bdl	bdl	bdl
NiO	0.02	0.00	0.00	0.01	0.14	0.04	0.09	0.01	0.01
ZnO	0.00	0.00	0.02	0.03	0.06	0.06	0.22	0.03	0.16
Total	100.81	99.89	99.83	100.08	99.09	99.95	99.08	100.21	99.58
O	3	3	3	4	4	4	4	4	4
Si	0.01	0.00	0.00	0.01	0.03	0.01	0.03	0.01	0.03
Ti	0.00	0.00	0.00	0.00	0.00	0.00	0.01	0.00	0.00
Al	1.97	1.99	1.99	1.96	1.95	1.97	1.96	1.96	1.94
Cr	0.00	0.00	0.00	0.00	0.00	0.00	0.00	0.00	0.00
Fe^{3+}				0.00	0.00	0.01	0.00	0.01	0.00
Fe^{2+}	0.01	0.01	0.01	0.59	0.59	0.58	0.61	0.58	0.60
Mn	0.00	0.00	0.00	0.00	0.00	0.00	0.00	0.00	0.00
Mg	0.00	0.00	0.00	0.42	0.41	0.42	0.37	0.43	0.41
Ca	0.00	0.00	0.00	0.00	0.01	0.00	0.01	0.00	0.01
Na	0.00	0.00	0.00	bdl	bdl	bdl	bdl	bdl	bdl
K	0.00	0.00	0.00	bdl	bdl	bdl	bdl	bdl	bdl
Ni	0.00	0.00	0.00	0.00	0.00	0.00	0.00	0.00	0.00
Zn	0.00	0.00	0.00	0.00	0.00	0.00	0.00	0.00	0.00
Total	2	2	2	3	3	3	3	3	3
X_{Mg}[b]				0.42	0.41	0.42	0.38	0.42	0.41

[a] bdl = below detection limit. [b] $X_{Mg} = Mg/(Mg + Fe^{2+})$.

be replaced by spinel, biotite, and other K–Al phases (mullite, feldspar, and K-feldspar) during the decomposition of phengite (e.g., Patiño Douce and Harris, 1998; Rushmer, 2001; Michaud et al., 2021). Importantly, silicate melts and glass were generally observed surrounding the spinel grains in these experiments (e.g., Patiño Douce and Harris, 1998; Rushmer, 2001; Devineau et al., 2006), which clearly indicates the formation of spinel + biotite assemblages by partial melting. The compositions of spinel (25.1 wt %– 27.0 wt % for FeO; 9.66 wt %–10.8 wt % for MgO) in the SPB symplectites from the Yanwo eclogites are similar to those of spinel (23.7 wt %–32.8 wt % for FeO; 7.28 wt %– 12.1 wt % for MgO) formed by the partial melting of phengite (e.g., Brearley and Rubie, 1990; Patiño Douce and Harris, 1998; Spicer et al., 2004), supporting the interpretation that the SPB symplectites are also the products of phengite melting. Similar symplectites of SPB in eclogites are also reported in other UHP terranes, such as the Bohemian Massif (Faryad et al., 2006); Papua New Guinea (Faryad et al.,

2019); and Tromsø Nappe, Norway (Janák et al., 2012), and were proved to form at high temperatures of 700–850 °C at 0.5–1.5 GPa, which are beyond the fluid-absent solidus in metabasalt system (Holland and Powell, 2001). Different from the CPB symplectites, no kyanite is found near the regions of the SPB symplectites, implying that the involvement of kyanite during the breakdown of phengite facilitates the formation of corundum instead of spinel. Thus, the replacement reaction of SPB symplectites can be concluded as follows: Ph→ Spl + Pl + Bt + melt.

The third type of symplectite (SP) develops around both the matrix paragonite and paragonite inclusions in omphacite. The symplectitic assemblage of spinel + plagioclase ± amphibole after paragonite has rarely been found in eclogites so far (Ferrando et al., 2005). Both the matrix paragonite and paragonite inclusions show obvious corroded structures (Fig. 6b–d). The Raman (Fig. 3f) and X-ray maps (Fig. 7) show that fine-grained vermicular spinel (up to 10 μm) grows perpendicular to the original paragonite grain

Table 2. The representative major element compositions of plagioclase in Yanwo eclogites (oxide concentrations in wt %).
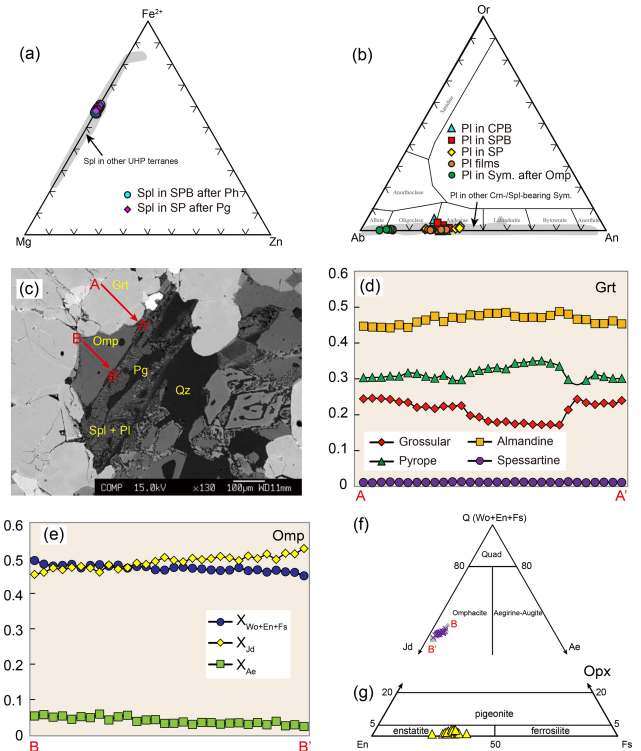
Mineral	Pl														
texture	In symplectites of CPB			In symplectites of SPB			In symplectites of SP			In symplectites after omphacite			Pl films		
SiO_2	59.06	59.05	57.56	58.44	59.00	59.13	56.20	58.79	61.81	65.40	66.71	65.09	59.54	60.86	59.42
TiO_2	0.08	0.13	0.14	0.00	0.04	0.11	0.02	0.05	0.05	0.05	0.00	0.04	0.01	0.01	0.70
Al_2O_3	25.70	26.32	27.27	25.86	25.95	25.17	27.28	25.76	24.19	20.54	19.91	21.62	25.19	25.28	25.02
Cr_2O_3	0.02	0.00	0.01	0.00	0.00	0.02	0.06	0.00	0.03	0.03	0.00	0.01	0.01	0.00	0.02
FeO	0.37	0.86	1.30	0.21	0.62	0.77	0.85	0.26	0.27	0.35	0.43	0.39	0.81	0.16	0.79
MnO	0.00	0.00	0.00	0.00	0.01	0.01	0.00	0.01	0.00	0.00	0.02	0.00	0.00	0.02	0.03
MgO	0.12	0.63	1.00	0.11	0.41	0.79	0.68	0.04	0.14	0.32	0.35	0.13	0.58	0.01	0.20
CaO	6.99	4.50	4.34	7.46	6.79	6.41	7.94	7.35	5.04	2.84	1.71	2.53	5.91	5.91	6.76
Na_2O	7.72	8.38	8.07	7.38	7.52	8.00	6.58	7.92	7.83	10.52	11.29	10.89	8.34	8.76	7.78
K_2O	0.19	0.74	0.99	0.20	0.42	0.67	0.21	0.10	0.09	0.11	0.03	0.06	0.42	0.08	0.07
NiO	0.01	0.02	0.00	0.00	0.00	0.00	0.00	0.00	0.00	0.01	0.00	0.02	0.00	0.00	0.00
Total	100.24	100.62	100.67	99.67	100.76	101.07	99.83	100.28	99.44	100.17	100.45	100.75	100.81	101.09	100.79
O	8	8	8	8	8	8	8	8	8	8	8	8	8	8	8
Si	2.64	2.63	2.57	2.62	2.62	2.63	2.53	2.63	2.75	2.89	2.93	2.86	2.65	2.68	2.64
Ti	0.00	0.00	0.00	0.00	0.00	0.00	0.00	0.00	0.00	0.00	0.00	0.00	0.00	0.00	0.02
Al	1.35	1.38	1.43	1.37	1.36	1.32	1.45	1.36	1.27	1.07	1.03	1.12	1.32	1.31	1.31
Cr	0.00	0.00	0.00	0.00	0.00	0.00	0.00	0.00	0.00	0.00	0.00	0.00	0.00	0.00	0.00
Fe^{2+}	0.01	0.03	0.05	0.01	0.02	0.03	0.03	0.01	0.01	0.01	0.02	0.01	0.03	0.01	0.03
Mn	0.00	0.00	0.00	0.00	0.00	0.00	0.00	0.00	0.00	0.00	0.00	0.00	0.00	0.00	0.00
Mg	0.01	0.01	0.07	0.01	0.03	0.05	0.05	0.00	0.01	0.02	0.00	0.01	0.04	0.00	0.01
Ca	0.33	0.33	0.21	0.36	0.32	0.31	0.38	0.35	0.24	0.13	0.08	0.12	0.28	0.28	0.32
Na	0.67	0.72	0.70	0.64	0.65	0.69	0.58	0.69	0.67	0.90	0.96	0.93	0.72	0.75	0.67
K	0.01	0.04	0.06	0.01	0.02	0.04	0.01	0.01	0.00	0.01	0.00	0.00	0.02	0.00	0.00
Ni	0.00	0.00	0.00	0.00	0.00	0.00	0.00	0.00	0.00	0.00	0.00	0.00	0.00	0.00	0.00
Total	5	5	5	5	5	5	5	5	5	5	5	5	5	5	5
An	0.33	0.22	0.22	0.35	0.33	0.30	0.39	0.34	0.26	0.13	0.08	0.11	0.27	0.27	0.32
Ab	0.66	0.74	0.73	0.63	0.65	0.67	0.59	0.66	0.73	0.87	0.92	0.88	0.70	0.73	0.67
Or	0.01	0.04	0.06	0.01	0.02	0.04	0.01	0.01	0.01	0.01	0.00	0.00	0.02	0.00	0.00

An: anorthite. Ab: albite. Or: orthoclase.
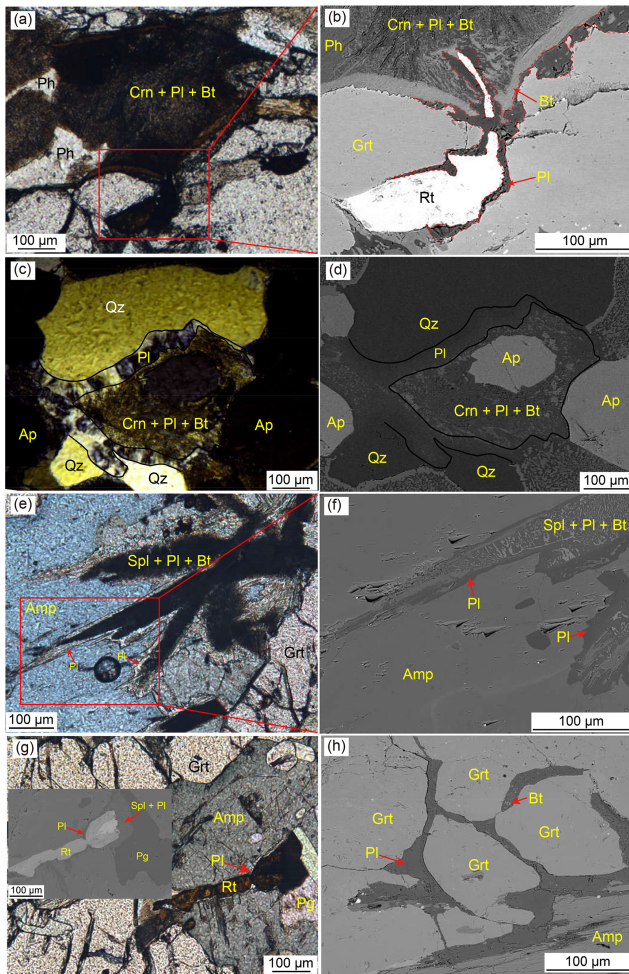
Figure 8. Photomicrographs **(a, c, e, g)** and BSE images **(b, d, f, h)** showing the melt textures in the studied eclogites (17YW3 and 17YW7). **(a–d)** In the CPB symplectite domains, elongated Na-rich plagioclase occurs as films distributed along quartz and rutile grain boundaries. **(e, f)** In the SPB symplectite domain, elongated Na-rich plagioclase occurs as films distributed along the boundaries of symplectite and amphibole grain boundaries. **(g)** In the SP symplectite domain, plagioclase with clear cuspate margins extends along the symplectite boundaries. **(h)** The intergrowth of plagioclase with fine-grained biotite distributes at the junction between garnet grains.

Figure 9. Compositions of spinel, plagioclase, garnet, omphacite, and orthopyroxene. Ternary diagrams showing compositions of spinel **(a)** and plagioclase **(b)**. Zoning profile of garnet **(d)** and omphacite **(e)** near the SP symplectite after paragonite **(c)**. The inset ternary diagram in **(e)** showing composition of omphacite **(f)**. Ternary diagram showing composition of orthopyroxene **(g)**. The shaded region in **(a)** represents the compositional range of spinel in global UHP terranes. The shaded region in **(b)** represents the compositional range of plagioclase in global UHP terranes. Data sources of spinel and plagioclase are from the references listed in Table 5.

boundary, indicating the growth of spinel at the expense of paragonite. The omphacite in contact with paragonite commonly shows embayment textures and serrated grain boundaries, suggesting that omphacite grains were partly consumed and may be involved in the reaction of SP symplectite formation (Fig. 6a–c). For example, the lower Mg, Ca, and Fe compositions of omphacite adjacent to the SP suggest that MgO, CaO, and FeO from omphacite were added into the products (Fig. 9e, f; Table S3). Thus, the reaction of SP formation can be concluded as follows: $Pg + Omp \rightarrow Spl + Pl \pm Amp + melt$.

In addition to these symplectites, several textures of partial melting and melt flow were observed in the eclogites (Fig. 8): (1) abundant fine films of plagioclase are observed to be distributed along the boundaries of the CPB and SPB symplectites with other minerals (e.g., quartz and rutile) (Fig. 8a–f). The films show typical tapered ends, which suggest consistently small dihedral angles (Fig. 8b, d). This textural feature is consistent with the presence of former silicate melts in HT metamorphic rocks (e.g., Brearley and Rubie, 1990; Holness et al., 2011; Vernon, 2011; Bartoli et al., 2013; Dokukina et al., 2021). The plagioclase moats are interpreted as textures of hydrous melt passing along the grain boundaries (Holness, 2011; Bartoli et al., 2013; Dokukina et al., 2021). (2) In the SP symplectite domain, plagioclase with clear cuspate margins extends along the symplectite boundaries (Fig. 8g). The cuspate-shaped areas of plagioclase have been regarded as the pools of crystallized melt that has penetrated along the surrounding minerals (e.g., Sawyer, 2001; Holness and Sawyer, 2008). The embayed shape of surrounding minerals

(e.g., Grt and Amp) could be caused by the corrosion during partial melting, according to Vernon (2011). (3) In other regions, the intergrowth of plagioclase with fine-grained biotite distributes at the junction between garnet grains (Fig. 8h). This texture is similar to the interstitial pockets of plagioclase (crystallized from a silicate melt) at quartz triple junctions in partially melted quartz-plagioclase rock (Holness, 2011). Thus, these textures, in line with the three types of symplectites, again support the interpretation that hydrous melt has been released during the breakdown of a hydrous phase (phengite or paragonite) into an anhydrous assemblage (corundum, spinel, and plagioclase) during slab exhumation.

5.2   Formation conditions of the symplectites

To constrain the conditions of distinct symplectites after muscovite (CPB, SPB, and SP) observed in the eclogites, phase equilibrium modeling was conducted in the Na_2O–CaO–K_2O–FeO–MgO–Al_2O_3–SiO_2–H_2O–Fe_2O_3 (NCKFMASHO) system. The P–T pseudosections were calculated using the Perple_X software (Connolly, 1990, 2009) and the internally consistent thermodynamic dataset of Holland and Powell (2011). Three P–T pseudosections (Figs. 10a, b and 11) were calculated, based on the effective bulk composition of CPB, SPB, and SP assemblages, respectively. The effective bulk compositions were estimated in terms of the abundance of minerals in symplectites and mineral composition (Table 3) using the methods of Godard and Mabit (1998) and Groppo et al. (2009). Fe_2O_3 content was calculated by integrating total FeO and ratio of X_{Fe3+} ($= Fe^{3+}/(Fe^{3+}+ Fe^{2+})$) ($= 0.12$; Bezos and Humler, 2005). The solid-solution models are as follows: garnet (White et al., 2007), clinopyroxene, epidote, spinel, orthopyroxene, sapphirine and chlorite (Holland and Powell, 1998), muscovite (Coggon and Holland, 2002), plagioclase (Holland and Powell, 2003), amphibole (Dale et al., 2005), biotite (Tajčmanová et al., 2009), and melt (Holland and Powell, 2001). As shown in Figs. 10a and b and 11, phengite and paragonite are stable at conditions of low temperatures and high pressures (phengite: $< 790\,°C$ and $> 0.9\,$GPa; paragonite: $< 750\,°C$ and $> 0.9\,$GPa). Kyanite is stable at a narrow temperature range of 720–770 °C when the pressure is $> 1.0\,$GPa. The solidus curve is present at $> 770\,°C$.

Considering that the three types of symplectites formed by the partial melting of muscovite, the occurrence of corundum + plagioclase + biotite + melt defines the P–T conditions of CPB symplectites after phengite at $> 0.7\,$GPa and $> 770\,$°C according to the pseudosection (Fig. 10a). The formation of SPB symplectites after phengite was constrained in the P–T range of $< 0.95\,$GPa and $> 770\,$°C (Fig. 10b). The assemblage of SP is stable in the P–T range of $< 1.0\,$GPa and $> 770\,$°C (Fig. 11). In addition, the isopleths of X_{Mg} in spinel and X_{Ca} ($= Ca/(Ca + Na)$) in plagioclase were calculated to further constrain the P–T conditions of symplectites. Based on the CPB assemblages and the X_{Ca} values in plagioclase
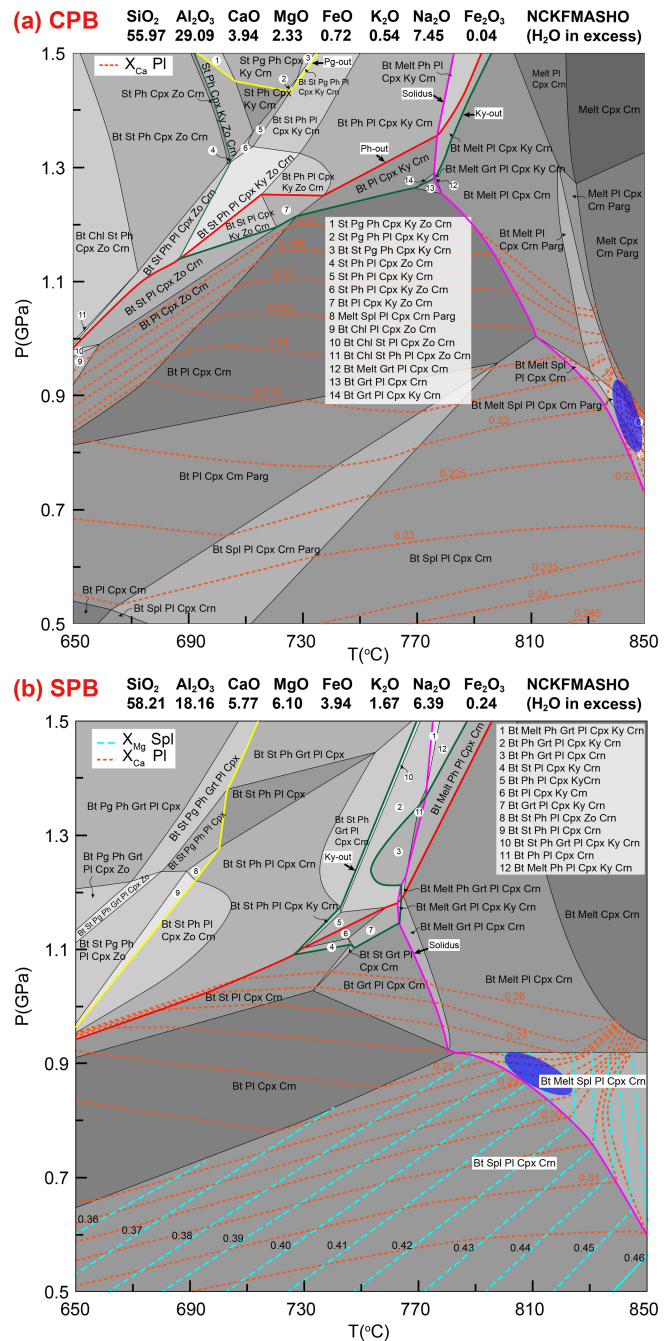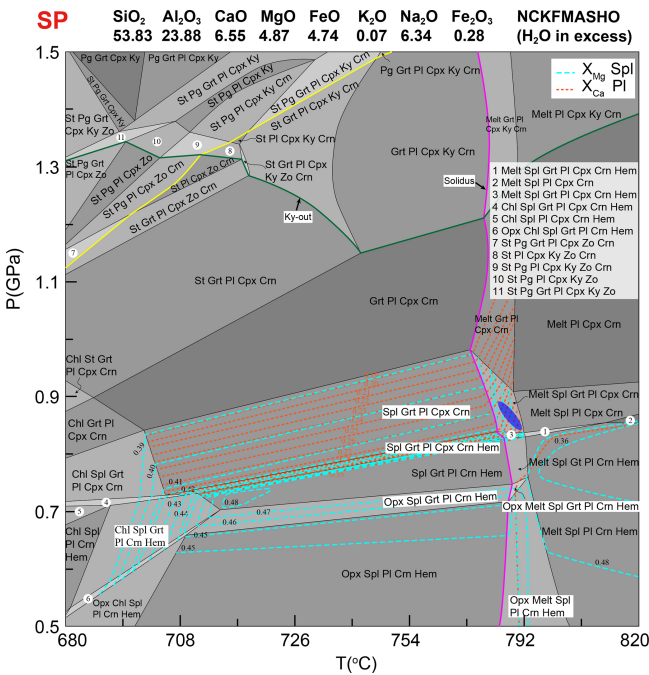

Figure 10. P–T pseudosection for the symplectites after phengite calculated in the NCKFMASHO system. The rock composition is given as molecule percentage (mol %) oxide. The green, red, yellow, and orange lines represent the stability curves of kyanite, phengite, paragonite, and solidus, respectively. X_{Mg} isopleths of spinel and X_{Ca} isopleths of plagioclase are shown. The blue regions show the P–T fields of the symplectites. **(a)** P–T pseudosection for the CPB symplectites after phengite. **(b)** P–T pseudosection for the SPB symplectites after phengite.

Table 3. The effective bulk compositions used for pseudosection calculations.

Microdomain	CPB	SPB	SP
Figure	Fig. 10a	Fig. 10b	Fig. 11
SiO_2 (wt %)	55.97	58.21	53.83
Al_2O_3	29.09	18.16	23.88
CaO	3.94	5.77	6.55
MgO	2.33	6.10	4.87
tot FeO	0.72	3.94	4.74
K_2O	0.54	1.67	0.07
Na_2O	7.45	6.39	6.34
Fe_2O_3	0.04	0.24	0.28

Figure 11. P–T pseudosection for the symplectite after paragonite calculated in the NCKFMASHO system. The rock composition is given as molecule percentage (mol %) oxide. The green, yellow, and orange lines represent the stability curves of kyanite, paragonite, and solidus, respectively. X_{Mg} isopleths of spinel and X_{Ca} isopleths of plagioclase are shown. The blue regions show the P–T field of the symplectites.

(0.22–0.33), P–T conditions of CPB symplectites were estimated to be 0.8–0.9 GPa and 830–850 °C (Fig. 10a). Based on the SPB assemblages, the X_{Mg} values of spinel (0.38–0.42), and the X_{Ca} values of plagioclase (0.26–0.35), the P–T conditions of SPB symplectites were estimated to be 0.8–0.9 GPa and 780–820 °C (Fig. 10b). Similarly, intersections of X_{Mg} in spinel (0.38–0.43) and X_{Ca} in plagioclase isopleths (0.26–0.39) place the P–T conditions of SP symplectites at 0.8–0.9 GPa and 770–800 °C (Fig. 11).

In summary, the three types of symplectites formed at similar HT conditions (0.8–0.9 GPa and 770–850 °C). It is thus reasonable to consider that these symplectites after phengite and paragonite developed at a same metamorphic stage during the exhumation of eclogites. Moreover, Opx-bearing symplectites after omphacite were found to coexist with the SP symplectites (Fig. 6d). Therefore, the P–T conditions of Opx-bearing symplectites were calculated using the Cpx–Opx solvus thermobarometers of Brey and Köhler (1990) and Taylor (1998). The lower limit of pressures for the eclogite-facies conditions in the Yanwo eclogites is ~ 1.5 GPa (Tang et al., 2021). Thus, temperatures at pressures ranging from 0.5 to 1.5 GPa were estimated. In terms of the compositions of clinopyroxene ($Di_{56.1–59.5}Jd_{3.8–6.7}Ae_{0.9–5.3}$) and orthopyroxene ($X_{Mg}$ values of 0.67–0.76), five groups of Cpx–Opx pairs yielded temperature ranges of 772–837 °C (Brey and Köhler, 1990) and 763–879 °C (Taylor, 1998), respectively (Table S5), which are in good agreement with those constrained by the phase equilibrium modeling. Therefore, we conclude that the formation of Crn-bearing and Spl-bearing symplectites after muscovite, as well as the development of Di + Opx + Pl symplectites after omphacite, all occur at the granulite-facies stage during exhumation.

5.3 Element exchange during symplectite formation

The Crn-bearing and Spl-bearing symplectites were formed by the replacement of phengite or paragonite. If muscovite is regarded as a reference, such a replacement process can be considered as occurring in open systems and involving element exchange or transfer. Quantifying the element exchange during the formation of symplectites is essential to understand the replacement processes. In this study, a mass balance method of Godard and Mabit (1998) was used to constrain the element gains or losses from the system.

The formation of the phengite pseudomorph (CPB and SPB) can be expressed as follows: CPB: 1 Ph $+X_i \rightarrow a_1$ Crn $+b_1$ Pl $+c_1$ Bt; SPB: 1 Ph $+X_i \rightarrow a_2$ Spl $+b_2$ Pl $+c_2$ Bt. Paragonite pseudomorph can be expressed as SP, 1 Pg $+X_i \rightarrow a_3$ Spl $+ b_3$ Pl, where $a_1, a_2, a_3, b_1, b_2, b_3, c_1$, and c_2 are stoichiometric coefficients and X_i is a vector ($X_{Si}, X_{Al}, \ldots, X_{Na}$), representing the quantity of the element i (Si, Al,..., Na) transferred between the muscovite system and its surroundings. If $X_i = 0$, the system is closed for the considered element i; otherwise, X_i represents the gain ($X_i > 0$) or the loss ($X_i < 0$) of the element.

According to Godard and Mabit (1998), X_i can be expressed by the following equation for each considered element i (taking the equation of the CPB symplectite for an example):
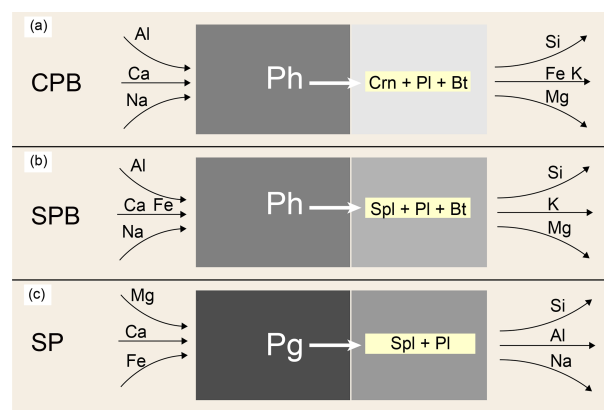
$$X_i = F_V V_{Ph} \left(\frac{X_{vol}^{Crn} N_i^{Crn}}{V_{Crn}} + \frac{X_{vol}^{Pl} N_i^{pl}}{V_{Pl}} + \frac{X_{vol}^{Bt} N_i^{Bt}}{V_{Bt}} \right) - N_i^{Ph}, \quad (1)$$

where Fv is the volumetric factor defined as (ΔV/V) +1, and V_M (e.g., $V_{Crn}, V_{Spl}, V_{Pl}, V_{Bt}$, and V_{Ph}) represents the mo-
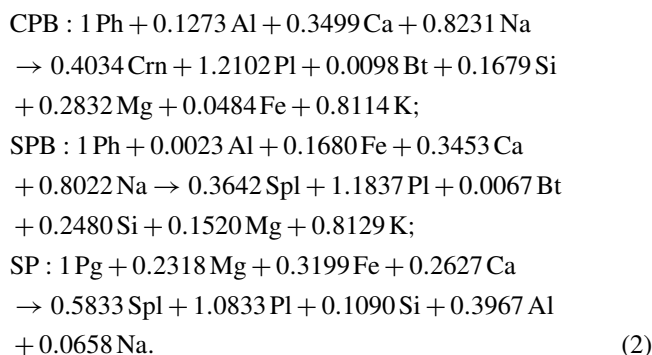
Table 4. Material transfer calculations for the symplectites after phengite and paragonite.

Type	Symplectites after Ph		Symplectites after Pg
	CPB	SPB	SP
Fv	2.02	1.82	1.67
X_{vol}^{Spl}	0	0.2	0.35
X_{vol}^{Crn}	0.2	0	0
X_{vol}^{Pl}	0.6	0.65	0.65
X_{vol}^{Bt}	0.2	0.15	0
X_{si}	−0.1679	−0.2480	−0.1090
X_{Al}	0.1273	0.0023	−0.3967
X_{Mg}	−0.2832	−0.1520	0.2318
X_{Fe}	−0.0484	0.1680	0.3199
X_{Ca}	0.3499	0.3453	0.2627
X_{Na}	0.8231	0.8022	−0.0658
X_{K}	−0.8114	−0.8129	
X_{O}	0	0	0
a	0.4034	0.3642	0.5833
b	1.2102	1.1837	1.0833
c	0.0098	0.0067	

Figure 12. Schematic view showing the element transfer during the formations of the CPB **(a)**, SPB **(b)**, and SP **(c)** symplectites in the studied eclogites.

lar volume of the considered mineral M, which is from Holland and Powell (1998). X_{vol}^{Crn}, X_{vol}^{Spl}, X_{vol}^{Pl}, and X_{vol}^{Bt} are the volumetric proportion of the products, which are obtained by estimating the mineral distributions (Table 4). N_i^M is the quantity of the element i in the mineral M, which is obtained by EPMA. In our calculation of mass transfer, eight elements (Si, Al, Mg, Fe, Ca, K, Na, and O) are considered, and then eight independent equations (α) with nine unknowns variables (X_{Si}, X_{Al}, X_{Mg}, X_{Fe}, X_{Ca}, X_{K}, X_{Na}, X_{O}, and Fv) are presented. There is probably an infinity of solutions because of the under-determined eight independent equations. It is commonly accepted that mass transfer needs to consume energy (Nakamura and Hirajima, 2000). Thus the most likely solution can be decided by minimizing the total mass transfer $\sum_i |X_i|$. After gaining the optimal Fv, the X_i can be calculated successively. The detailed calculation process has been described in Godard and Mabit (1998). The optimal Fv, X_i, and volumetric proportion of the products are listed in Table 4.

A similar calculation process is applied to the SPB and SP symplectites. The results are listed in Table 4 and shown in Fig. 12. Based on mass transfer calculations, the estimated reactions are

$$CPB : 1\,Ph + 0.1273\,Al + 0.3499\,Ca + 0.8231\,Na$$
$$\rightarrow 0.4034\,Crn + 1.2102\,Pl + 0.0098\,Bt + 0.1679\,Si$$
$$+ 0.2832\,Mg + 0.0484\,Fe + 0.8114\,K;$$
$$SPB : 1\,Ph + 0.0023\,Al + 0.1680\,Fe + 0.3453\,Ca$$
$$+ 0.8022\,Na \rightarrow 0.3642\,Spl + 1.1837\,Pl + 0.0067\,Bt$$
$$+ 0.2480\,Si + 0.1520\,Mg + 0.8129\,K;$$
$$SP : 1\,Pg + 0.2318\,Mg + 0.3199\,Fe + 0.2627\,Ca$$
$$\rightarrow 0.5833\,Spl + 1.0833\,Pl + 0.1090\,Si + 0.3967\,Al$$
$$+ 0.0658\,Na. \qquad (2)$$

The results indicate that the formations of both the CPB and SPB symplectites require the gain of Al, Ca, and Na from its surroundings and loss of Si, Mg, and K (Fig. 12a, b). Al, Ca, and Na are most likely derived from the adjacent garnet and omphacite near the symplectites. In contrast, the replacement of paragonite by the SP symplectites needs the external input of Mg, Ca, and Fe and removal of Si, Al, and Na to the surroundings (Fig. 12c). Omphacite is the most likely reactant to provide Mg, Ca, and Fe for the formation of SP symplectites because the omphacite near the SP symplectites shows lower Mg, Ca, and Fe contents than that far away from SP (Fig. 9e, f). The replacement of muscovite by the symplectites and the element transfer are mainly by a dissolution–precipitation metasomatic process (e.g., Anderson and Moecher, 2007; Putnis et al., 2009; Martin and Duchêne, 2015; Guo et al., 2012, 2019, 2022b).
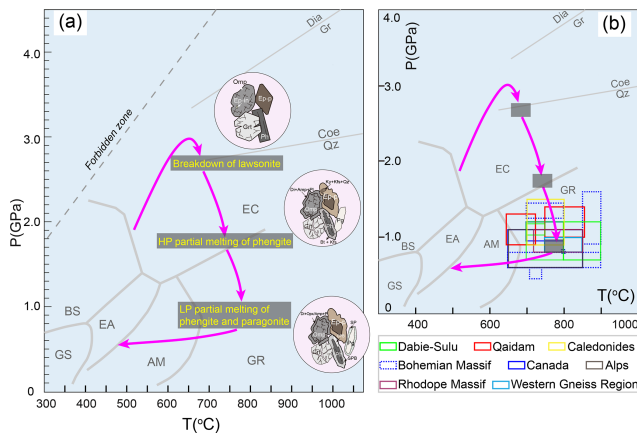
Figure 13. (a) The clockwise P–T path of the Yanwo eclogite (modified after Tang et al., 2021). Schematic sketch in the circle (not to scale) showing the evolution of mineral assemblages in eclogite. **(b)** Summary of P–T conditions of the Crn- and Spl-bearing symplectites reported in global UHP terranes. The detailed P–T data are presented in Table 5.

5.4   Comparison with Crn- and Spl-bearing symplectites in global UHP terranes

In fact, Crn- and Spl-bearing symplectites after eclogite-facies minerals have been reported in many other UHP metamorphic terranes. Figure 13 and Table 5 summarize the UHP terranes where Crn- and Spl-bearing symplectites have been found, including the Sulu terrane (Nakamura and Hirajima, 2000), the north Dabie complex (Groppo et al., 2015), and the north Qaidam (Zhang et al., 2009b) of China; the Armorican Massif in the Alps (Godard and Mabit, 1998); the Bohemian Massif of Germany (Faryad et al., 2006; Tajčmanová et al., 2007; Štípská et al., 2010); Sveconorwegian (Möller, 1998) and Saskatchewan of Canada (Baldwin et al., 2015); the Rhodope Massif of Greece (e.g., Moulas et al., 2013); the Caledonides of Greenland (Elvevold and Gilotti, 2000); and the Western Gneiss Region of Norway (Janák et al., 2012). Petrological studies indicate that most of these symplectites formed at relatively low-pressure (0.6–1.0 GPa) and high-temperature conditions (> 750 °C) (Fig. 13b), which is in agreement with our estimations. Such a result also demonstrates that the Crn- and Spl-bearing assemblages exclusively formed at the granulite-facies or HT amphibolite-facies stage during the exhumation of eclogites. The widespread occurrence of Crn- and Spl-bearing symplectites in global UHP terranes indicates that most exhumed continental slabs may have experienced a heating stage during decompression, especially for those with large sizes (e.g., Kylander-Clark et al., 2012; Liu et al., 2015; Faryad and Cuthbert, 2020; Wang et al., 2023).

The compositions of spinel in the symplectites of SPB and SP fall in the composition range of symplectitic spinel from these previously reported UHP terranes (Fig. 9a). Mean-while, the composition of plagioclase in the three types of symplectite also falls in the composition range of plagioclase in symplectites from these reported UHP terranes (Fig. 9b). However, different from the symplectites in this study, the previously reported symplectites from other UHP terranes were typically formed by the breakdown of Al-rich anhydrous minerals (e.g., kyanite, omphacite, and garnet) (Table 5). This process always produces the anhydrous symplectite assemblages. In contrast, our new results on the Dabie eclogites reveal that the breakdown of Al-rich hydrous minerals (muscovite) can also produce the Crn-bearing and Spl-bearing assemblages. Importantly, the formation of the symplectites is caused by partial melting, which generated hydrous phases (e.g., biotite) in the products and led to the production and flow of silicate melts at HT conditions. Thus, reactants may play a key role in the formation of different mineral assemblages and the mechanism of metamorphic reactions during the formation of Crn- and Spl-bearing symplectites.

6   Implications for multiple episodes of partial melting of exhumed slab

Partial melting of HP–UHP metamorphic rocks plays a key role in the geodynamic evolution and chemical exchange of subduction zones. Our new results demonstrate that the development of Crn- and Spl-bearing symplectites in the UHP eclogites is related to the HT metamorphic overprint and partial melting at LP stages. This result, in combination with Tang et al. (2021), reveals at least two episodes of melting in the Yanwo eclogites during the retrograde process (Fig. 13a): (1) the first episode of partial melting occurred at the HP stage ($\sim$ 1.5–2.0 GPa and 700–750 °C) and was induced by the breakdown of phengite via the reaction Ph + Qz + H$_2$O → Ky + Kfs + melt. Water, which is derived from the breakdown of lawsonite (e.g., Guo et al., 2013, 2015), was involved in the reaction. This process resulted in the development of MSIs in eclogite minerals (e.g., garnet) and some veinlets of Ep + Pl + Kfs in the vein (Tang et al., 2021). (2) As the pressure further decreases to 0.8–0.9 GPa, the second episode of partial melting of phengite and paragonite took place at 770–850 °C, via the following dehydration melting reactions: Ph + Ky→ Crn + Pl + Bt + melt, Ph→ Spl + Pl + Bt + melt, and Pg + Omp→ Spl + Pl ± Amp + melt. This process formed low-pressure Crn- and Spl-bearing symplectites. We thus stress that the eclogites may experience multiple episodes of partial melting (HP vs. LP) during the exhumation process. Multiple episodes of partial melting of HP–UHP rocks were also found in Sulu terrane in China (Wang et al., 2017, 2023), the Kokshetau in Kazakhstan (Korsakov and Hermann, 2006), and the Caledonides in Greenland (Gilotti et al., 2014). Recognizing and characterizing these different melting events in the eclogites is the key to understand the thermal evolution history of exhumed slabs.

Table 5. Summary of P–T conditions of the Crn- and Spl-bearing symplectites reported in global UHP terranes.

Region	Locality	Lithology/rock type	Corona/symplectite	P–T conditions	Metamorphism	Formation mechanism	References
China	Rongcheng, Sulu	Eclogite	Spl + Pl + Crn	0.7–1.2 GPa; 700–800 °C	Granulite facies	Breakdown of Ky	Nakamura and Hirajima (2000)
	Donghai, Sulu	Eclogite	Crn + Pl ± St	~1.1 GPa; 700–750 °C	–*	Breakdown of Ky + Grt	Enami and Zang (1988)
	Luotian, north	Eclogite	Spl + Pl	1.0–1.2 GPa; 800–900 °C	Granulite facies	Breakdown of Ky	Groppo et al. (2015)
	Dabie complex	Eclogite	Spl + Pl ± Mt	0.7–1.2 GPa; > 830 °C	Granulite facies	Breakdown of Ky	Deng et al. (2021)
	Shaliuhe, north Qaidam	Kyanite eclogite	Spl + Pl	0.9–1.3 GPa; 645–725 °C	Granulite and amphibolite facies	Breakdown of Ky	Zhang et al. (2009b)
Alps	Gorduno	Kyanite eclogite	Crn + Spl + Pl	0.6 ± 0.1 GPa; 675 ± 25 °C	LP–HT	Breakdown of Ky + Omp	Brouwer and Engi (2005)
	Monte Duria	Kyanite eclogite	Spl ± Crn + Pl ± Sapp	0.8–1.0 GPa; 850 °C	Granulite facies	Breakdown of Ky	Tumiati et al. (2018)
	Golfo Aranci NE Sardinia	Kyanite eclogite	Crn + Pl + Spl + Sapp	0.9–1.1 GPa; 650–850 °C	Granulite facies	Breakdown of Ky + Grt	Cruciani et al. (2019)
	NE Sardinia, Italy	Eclogite	Crn + Spl + Pl + Sapp	~1.0 GPa; 700–800 °C	Granulite facies	Breakdown of Ky + Omp	Giacomini et al. (2005)
	The Armorican Massif, France	Qz-free eclogite	Crn + Spl + Pl + Sapp	–	LP–HT	Breakdown of Ky	Godard and Mabit (1998)
Bohemian Massif,	Moldanubian domain	Granulite	Spl + Pl + Bt	0.4–0.6 GPa; 710–740 °C	LP	Breakdown of Ky	Tajčmanová et al. (2007)
Germany	Blansky les massif	Granulite	Crn + Spl + Pl	0.8 GPa; 800 °C	Granulite facies	Breakdown of Ky	Štípská et al. (2010)
	Světlík	Retrogressed	Spl + Pl + Bt	1.2–1.5 GPa; 700–800 °C	Granulite facies	Breakdown of Ph	Faryad et al. (2006)
		eclogite	Spl + Pl ± Sapp	1.2–1.5 GPa; 700–800 °C	Granulite facies	Breakdown of Ky + Grt	Faryad et al. (2006)
Canada	Saskatchewan	Granulite	Crn + Spl + Pl + Sapp	0.6–1.1 GPa; 650–850 °C	LP granulite facies	Breakdown of Ky + matrix	Baldwin et al. (2015)
	Sveconorwegian	Eclogite	Crn + Spl + Pl + Sapp	0.9–1.2 GPa; 705–795 °C	Upper amphibolite facies	Breakdown of Ky + Grt	Möller (1998)
Greenland Caledonides	Weinschenk Island	Kyanite eclogite	Crn + Spl + Pl + Sapp	< 1.6 GPa; 700–800 °C	Upper amphibolite/granulite facies	Breakdown of Ky	Elvevold and Gilotti (2000)
The Rhodope Massif in Greece	Greek Rhodope	Kyanite eclogite	Spl + Pl + Sapp ± Crn	< 1.0 GPa; ~720 °C	Amphibolite facies	Breakdown of Ky + Grt	Liati and Seidel (1994), Moulas et al. (2013)
	Bulgaria	Kyanite eclogite	Crn + Spl + Pl	~1.1 GPa; 800–850 °C	HP granulite facies	Breakdown of Ky	Janák et al. (2011)
Western Gneiss	Roan peninsula	Granulite	Crn + Spl + Pl + Opx + Sapp	1.0–1.3 GPa; ~800 °C	Granulite facies	Breakdown of Ky + Cpx	Johansson and Moller (1986)
region, Norway	Tromsø Nappe	Phengite eclogite	Spl + Pl + Bt	0.5–0.7 GPa; 700–800 °C	HT	Breakdown of Ph	Janák et al. (2012)

* No effective data.

The occurrence of Crn- and Spl-bearing symplectites replacing muscovite is a potential mineralogical indicator of LP partial melting in exhumed UHP eclogites.

Clearly, kyanite plays a different role in the two episodes of melting. During the HP stage, kyanite can be regarded as a peritectic product of partial melting (Tang et al., 2021), whereas during the LP stage, kyanite is a reactant that is involved in the melting reactions (Fig. 4a–c). This conclusion is also consistent with the experimental results (e.g., Skjerlie and Patiño Douce, 2002; Liu et al., 2009), which indicate that HP partial melting of eclogites (> 1.8–2.0 GPa) typically produces kyanite, whereas the LP (< 1.8 GPa) partial melting will consume kyanite. Thus, clarifying the behavior of kyanite during partial melting, based on the textural characteristics, can be used to distinguish the different episodes of the melting process.

7   Conclusions

Three types of Crn- and Spl-bearing symplectites in the Dabie UHP eclogites, including CPB (Crn + Pl + Bt), SPB (Spl + Pl + Bt), and SP (Spl + Pl) symplectites, were recognized and studied. The combination of petrology, mineral compositions, and thermodynamic modeling reveals that all the three types of symplectites formed by the breakdown of muscovite via the partial melting at the HT metamorphic stage during the exhumation process (0.8–0.9 GPa) of the UHP eclogites. The CPB and SPB symplectites formed by the partial melting of phengite at 780–850 °C, whereas the SP symplectite formed by the partial melting of paragonite at 770–800 °C. Mass balance calculations indicate that the formations of CPB and SPB symplectites require the gain of extra Al, Ca, and Na into the phengite regions and the loss of Si, Mg, and K from phengite. In contrast, the formation of SP symplectites is accompanied by the gain of Mg, Ca, and Fe into paragonite regions and by the loss of Si, Al, and Na to surrounding minerals. The integration of present results and investigations on Crn- and Spl-bearing symplectites from other UHP terranes demonstrates that such symplectites can be generated by the breakdown of both anhydrous and hydrous minerals. However, the breakdown of hydrous minerals typically produces hydrous phases and releases silicate melts. This study indicates that multiple episodes of partial melting events (HP vs. LP) may occur during the exhumation of a subducted UHP slab. By summarizing the P–T conditions of the Crn- and Spl-bearing symplectites in global UHP terranes, we stress that most of exhumed UHP slabs may experience a common heating stage during ascension to crustal depth.

Data availability. All data derived from this research are presented in the enclosed tables, figures, and Supplement.

Author contributions. SG collected the samples and designed the study. PT carried out detailed petrography, mineral chemistry, phase equilibrium modeling, and mass balance calculations. SG and PT interpreted the data and prepared the manuscript.

Competing interests. The contact author has declared that neither of the authors has any competing interests.

Disclaimer. Publisher's note: Copernicus Publications remains neutral with regard to jurisdictional claims in published maps and institutional affiliations.

Review statement. This paper was edited by Dejan Prelevic and reviewed by Songjie Wang, Dražen Balen, and one anonymous referee.

References

Anderson, E. D. and Moecher, D. P.: Omphacite breakdown reactions and relation to eclogite exhumation rates, Contrib. Mineral. Petr., 154, 253–277, https://doi.org/10.1007/s00410-007-0192-x, 2007.

Armstrong, J. T.: Microbeam Analysis, San Francisco Prc., 4, 177–200, 1995.

Awalt, M. B. and Whitney, D. L.: Petrogenesis of kyanite- and corundum-bearing mafic granulite in a meta-ophiolite, SE Turkey, J. Metamorph. Geol., 36, 881–904, https://doi.org/10.1111/jmg.12317, 2018.

Baldwin, J. A., Powell, R., White, R. W., and Štípská, P.: Using calculated chemical potential relationships to account for replacement of kyanite by symplectite in high pressure granulites, J. Metamorph. Geol., 33, 311–330, https://doi.org/10.1111/jmg.12122, 2015.

Bartoli, O., Cesare B, Poli. S., Bodnar, R. J., Acosta-Vigil, A., Frezzotti, M. L., and Meli, S.: Recovering the composition of melt and the fluid regime at the onset of crustal anatexis and S-type granite formation, Geology, 41, 115–118, https://doi.org/10.1130/G33455.1, 2013.

Bezos, A. and Humler, E.: The Fe3+/ΣFe ratios of MORB glasses and their implications for mantle melting, Geochim. Cosmochim. Acta, 69, 711–725, https://doi.org/10.1016/j.gca.2004.07.026, 2005.

Brearley, A. J. and Rubie, D. C.: Effects of H_2O on the disequilibrium breakdown of muscovite + quartz, J. Petrol., 31, 925–956, https://doi.org/10.1093/petrology/31.4.925, 1990.

Brey, G. P. and Köhler, T.: Geothermobarometry in 4-phase lherzolites. 2. New thermobarometers, and practical assessment of existing thermobarometers, J. Petrol., 31, 1353–1378, https://doi.org/10.1093/petrology/31.6.1353, 1990.

Brown, M., Korhonen, F. J., and Siddoway, C. S.: Organizing melt flow through the crust, Elements, 7, 261–266, https://doi.org/10.2113/gselements.7.4.261, 2011.

Cao, W. T., Massonne, H. J., and Liang, X.: Partial melting due to breakdown of phengite and amphibole in retrogressed eclogite of deep Precambrian crust: An example from the Algonquin terrane, western Grenville Province, Canada, Precambr. Res., 352, 105965, https://doi.org/10.1016/j.precamres.2020.105965, 2021.

Chen, Y. X., Zheng, Y. F., Gao, X. Y. and Hu, Z. C.: Multiphase solid inclusions in zoisite-bearing eclogite: evidence for partial melting of ultrahigh-pressure metamorphic rocks during continental collision, Lithos, 200–201, 1–21, https://doi.org/10.1016/j.lithos.2014.04.004, 2014.

Coggon, R. and Holland, T. J. B.: Mixing properties of phengitic micas and revised garnet-phengite thermobarometers, J. Metamorph. Geol., 20, 683–696, https://doi.org/10.1046/j.1525-1314.2002.00395.x, 2002.

Connolly, J. A. D.: Multivariable phase-diagrams: an algorithm based on generalized thermodynamics, Am. J. Sci., 290, 666–718, https://doi.org/10.2475/ajs.290.6.666, 1990.

Connolly, J. A. D.: The geodynamic equation of state: what and how, Geochem. Geophy. Geosy., https://doi.org/10 Q10014, 2009.

Cruciani, G., Franceschelli, M., Scodina, M., and Puxeddu, M.: Garnet zoning in kyanite©/bearing eclogite from Golfo Aranci: New data on the early prograde P–T evolution in NE Sardinia, Italy, Geol. J., 54, 190–205, https://doi.org/10.1002/gj.3169, 2019.

Dale, J., Powell, R., White, R. W., Elmer, F. L., and Holland, J. B.: A thermodynamic model for Ca–Na clinoamphiboles in Na2O–CaO–FeO–MgO–Al2O3–SiO2–H2O –O for petrological calculations, J. Metamorph Geol., 23, 771–791, https://doi.org/10.1111/j.1525-1314.2005.00609.x, 2005.

Deng, L. P., Liu, Y. C., Yang, Y., Groppo, C., Rolfo, F., and Gu, X. F.: Anatexis of high-T eclogites in the Dabie orogen triggered by exhumation and post-orogenic collapse, Eur. J. Mineral., 31, 889–903, https://doi.org/10.1127/ejm/2019/0031-2884, 2019.

Devineau, K., Devouard, B., Villieras, F., Faure, F., Devidal, J. L., and Kohler, A.: Evolution of product phase as-

semblages during thermal decomposition of muscovite under strong disequilibrium conditions, Am. Mineral., 91, 413–424, https://doi.org/10.2138/am.2006.1933, 2006.

Dokukina, K. A., Mints, M. V., and Konilov, A. N.: Melting of eclogite facies sedimentary rocks in the Belomorian Eclogite Province, Russia, J. Metamorph. Geol., 35, 435–451, https://doi.org/10.1111/jmg.12239, 2017.

Dokukina, K., Mints M, V., Khubanov, V. B., Sheshukov, V. S., Konilov, A. N., Bayanova, T. B., Kaulina, T. V., Golunova, M. A., Dokukin, P. A., Okina, O. I., Van, K. V., Yudin, D. S., Travin, A. V., Zaitsev, A. V., Kosorukov, V. L., Pozhilenko, V. I., and Golovanova, T. I.: Early Palaeoproterozoic granulite-facies metamorphism and partial melting of eclogite-facies rocks in the Salma association, eastern Fennoscandian Shield, Russia, Precambr. Res., 361, 106260, https://doi.org/10.1016/j.precamres.2021.106260, 2021.

Elvevold, S. and Gilotti, J. A.: Pressure–temperature evolution of retrogressed kyanite eclogites, Weinschenk Island, North–East Greenland Caledonides, Lithos, 53, 127–147, https://doi.org/10.1016/S0024-4937(00)00014-1, 2000.

Faryad, S. W. and Cuthbert, S. J.: High-temperature overprint in (U)HPM rocks exhumed from subduction zones; A product of isothermal decompression or a consequence of slab break-off (slab rollback)? Earth-Science Reviews, 103108, https://doi.org/10.1016/j.earscirev.2020.103108, 2020.

Faryad, S. W., Perraki, M., and Vrána, S.: P–T evolution and reaction textures in retrogressed eclogites from Svetlik, the Moldanubian Zone (Czech Republic), Miner. And. Petrol., 88, 297–319, https://doi.org/10.1007/s00710-006-0142-8, 2006.

Faryad, S. W., Kachlík, V., Sláma, J., and Hoinkes, G.: Implication of corona formation in a metatroctolite to the granulite facies overprint of HP–UHP rocks in the Moldanubian Zone (Bohemian Massif), J. Metamorph. Geol., 33, 295–310, https://doi.org/10.1111/jmg.12121, 2015.

Faryad, S. W., Baldwin, S. L., Jedlicka, R., and Ježek, J.: Two-stage garnet growth in coesite eclogite from the southeastern Papua New Guinea (U)HP terrane and its geodynamic significance. Contrib. Mineral. Petrol., 174, 73, https://doi.org/10.1007/s00410-019-1612-4, 2019.

Faure, M., Lin, W., Schärer, U., Shu, L., Sun, Y., and Arnaud, N.: Continental subduction and exhumation of UHP rocks. Structural and geochronological insights from the Dabieshan (East China), Lithos, 70, 213–241, https://doi.org/10.1016/S0024-4937(03)00100-2, 2003.

Ferrando, S., Frezzotti, M. L., Dallai, L., and Compagnoni, R.: Multiphase solid inclusions in UHP rocks (Su–Lu, China): Remnants of supercritical silicate-rich aqueous fluids released during continental subduction, Chem. Geol., 223, 68–81, https://doi.org/10.1016/j.chemgeo.2005.01.029, 2005.

Ferrero, S., Ziemann, M. A., Angel, R. J., O'Brien, P. J., and Wunder, B.: Kumdykolite, kokchetavite, and cristobalite crystallized in nanogranites from felsic granulites, Orlica-Snieznik Dome (Bohemian Massif): not evidence for ultrahigh-pressure conditions, Contrib. Mineral. Petrol., 171, 3, https://doi.org/10.1007/s00410-015-1220-x, 2016.

Gao, X. Y., Zheng, Y. F., and Chen, Y. X.: Dehydration melting of ultrahigh-pressure eclogite in the Dabie orogen: evidence from multiphase solid inclusions in garnet, J. Metamorph. Geol.,

30, 193–212, https://doi.org/10.1111/j.1525-1314.2011.00962.x, 2012.

Gao, X. Y., Chen, Y. X., and Zhang, Q. Q.: Multiphase solid inclusions in ultrahigh-pressure metamorphic rocks: A snapshot of anatectic melts during continental collision, J. Asian. Earth. Sci., 145, 192–204, https://doi.org/10.1016/j.jseaes.2017.03.036, 2017.

Giacomini, F., Bomparola, R. M., and Ghezzo, C.: Petrology and geochronology of metabasites with eclogite facies relics from NE Sardinia: constraints for the Palaeozoic evolution of Southern Europe, Lithos, 82, 221–248, https://doi.org/10.1016/j.lithos.2004.12.013, 2005.

Gilotti, J. A., McClelland, W. C., and Wooden, J. L.: Zircon captures exhumation of an ultrahigh-pressure terrane, North-East Greenland Caledonides, Gondwana Res., 25, 235–256, https://doi.org/10.1016/j.gr.2013.03.018, 2014.

Godard, G. and Mabit, J. L.: Peraluminous sapphirine formed during retrogression of a kyanite-bearing eclogite from Pays de LeÂon, Armorican Massif, France, Lithos, 43, 15–29, https://doi.org/10.1016/S0024-4937(98)00004-8, 1998.

Gordon, S. M., Little, T. A., Hacker, B. R., Bowring, S. A., Korchinski, M., Baldwin, S. L., and Kylander-Clark, A. R. C.: Multi-stage exhumation of young UHP-HP rocks: Timescales of melt crystallization in the D' Entrecasteaux Islands, southeastern Papua New Guinea, Earth. Planet. Sc. Lett., 351–352, 237–246, https://doi.org/10.1016/j.epsl.2012.07.014, 2012.

Guo, S., Ye, K., Chen, Y., Liu, J. B., Mao, Q., and Ma, Y. G.: Fluid–rock interaction and element mobilization in UHP metabasalt: Constraints from an omphacite–epidote vein and host eclogites in the Dabie orogen, Lithos, 136–139, 145–167, https://doi.org/10.1016/j.lithos.2011.11.008, 2012.

Guo, S., Ye, K., Wu, T. F., Chen, Y., Yang, Y. H., Zhang, L. M., Liu, J. B., Mao, Q., and Ma, Y. G.: A potential method to confirm the previous existence of lawsonite in eclogite: the mass imbalance of Sr and LREEs in multistage epidote (Ganghe, Dabie UHP terrane), J. Metamorph. Geol., 4, 415–435, https://doi.org/10.1111/jmg.12027, 2013.

Guo, S., Chen, Y., Ye, K., Su, B., Yang, Y. H., Zhang, L. M., Liu, J. B., and Mao, Q.: Formation of multiple high-pressure veins in ultrahigh-pressure eclogite (Hualiangting, Dabie terrane, China): Fluid source, element transfer, and closed-system metamorphic veining, Chem. Geol., 417, 238–260, https://doi.org/10.1016/j.chemgeo.2015.10.006, 2015.

Guo, S., Zhao, K. D., John, T., Tang, P., Chen, Y., and Su, B.: Metasomatic flow of metacarbonate-derived fluids carrying isotopically heavy boron in continental subduction zones: Insights from tourmaline-bearing ultra-high pressure eclogites and veins (Dabie terrane, eastern China), Geochim. Cosmochim. Acta, 159–200, https://doi.org/10.1016/j.gca.2019.03.013, 2019.

Guo, S., Hermann, J., Tang, P., Chu, X., Chen, Y., and Su, B.: Formation of carbon-bearing silicate melts by melt-metacarbonate interaction at convergent plate margins, Earth. Planet. Sc. Lett., 597, 117816, https://doi.org/10.1016/j.epsl.2022.117816, 2022a.

Guo, S., Su, B., John, T., Zhao, K. D., Tang, P., Chen, Y., and Li, Y. B.: Boron release and transfer induced by phengite breakdown in subducted impure metacarbonates, Lithos, 408–409, 16548, https://doi.org/10.1016/j.lithos.2021.106548, 2022b.

Goss, A. R. and Kay, S. M.: Steep REE patterns and enriched Pb isotopes in southern Central American arc magmas: Evidence

for forearc subduction erosion?, Geochem. Geophy. Geosy., 7, Q05016, https://doi.org/10.1029/2005GC001163, 2006.

Groppo, C., Beltrando, M., and Compagnoni, R.: The P-T path of the ultra-high pressure Lago Di Cignana and adjoining high-pressure meta-ophiolitic units: insights into the evolution of the subducting Tethyan slab, J. Metamorph. Geol., 27, 207–231, https://doi.org/10.1111/j.1525-1314.2009.00814.x, 2009.

Groppo, C., Rolfo, F., Liu, Y. C., Deng, L. P., and Wang, A. D.: P–T evolution of elusive UHP eclogites from the Luotian dome (North Dabie Zone, China): How far can the thermodynamic modeling lead us?, Lithos, 226, 183–200, https://doi.org/10.1016/j.lithos.2014.11.013, 2015.

Hermann, J., Spandler, C., Hack, A., and Korsakov, A. V.: Aqueous fluids and hydrous melts in high-pressure and ultra-high pressure rocks: implications for element transfer in subduction zones, Lithos, 92, 399–417, https://doi.org/10.1016/j.lithos.2006.03.055, 2006.

Holland, T. and Powell, R.: An internally consistent thermodynamic data set for phases of petrological interest, J. Metamorph. Geol., 16, 309–343, https://doi.org/10.1111/J.1525-1314.1998.00140.X, 1998.

Holland, T. J. B. and Powell, R.: Calculation of phase relations involving haplogranitic melts using an internally consistent thermodynamic dataset, J. Petrol., 42, 673–683, https://doi.org/10.1093/petrology/42.4.673, 2001.

Holland, T. and Powell, R.: Activity-composition relations for phases in petrological calculations: an asymmetric multicomponent formulation, Contrib. Mineral. Petr., 145, 492–501, https://doi.org/10.1007/s00410-003-0464-z, 2003.

Holland, T. and Powell, R.: An improved and extended internally consistent thermodynamic dataset for phases of petrological interest, involving a new equation of state for solids, J. Metamorph. Geol., 29, 333–383, https://doi.org/10.1111/j.1525-1314.2010.00923.x, 2011.

Holness, M. B. and Sawyer, E. W.: On the pseudomorphing of melt-filled pores during the crystallization of migmatites, J. Petrol., 49, 1343–1363, https://doi.org/10.1093/petrology/egn028, 2008.

Holness, M. B., Cesare, B., and Sawyer, E. W.: Melted Rocks under the Microscope: Microstructures and Their Interpretation, Elements. 7, 247–252. https://doi.org/10.2113/gselements.7.4.247, 2011.

Janák, M., Froitzheim, N., Georgiev, N., Nagel, T., and Sarov, S.: P-T evolution of kyanite eclogite from the Pirin Mountains (SW Bulgaria): implications for the Rhodope UHP Metamorphic Province, J. Metamorph. Geol., 29, 317–332, https://doi.org/10.1111/J.1525-1314.2010.00920.X, 2011.

Janák, M., Ravna, E. J. K., and Kullerud, K.: Constraining peak P–T conditions in UHP eclogites: calculated phase equilibria in kyanite- and phengite-bearing eclogite of the Tromsø Nappe, Norway, J. Metamorph. Geol., 30, 377–396, https://doi.org/10.1111/j.1525-1314.2011.00971.x, 2012.

Johansson, L. and Möller, C.: Formation of sapphirine during retrogression of a basic high-pressure granulite, Roan, Western Gneiss Region, Norway, Contrib. Mineral. Petr., 94, 29–41, https://doi.org/10.1007/BF00371223, 1986.

Korsakov, A. V. and Hermann, J.: Silicate and carbonate melt inclusions associated with diamonds in deeply subducted carbonate rocks, Earth. Planet. Sc. Lett., 241, 104–118, https://doi.org/10.1016/j.epsl.2005.10.037, 2006.

Kylander-Clark, A. R. C., Hacker, B. R., and Mattinson, C.G.: Size and exhumation rate of ultrahigh-pressure terranes linked to orogenic stage, Earth. Planet. Sc. Lett., 321, 115–120, https://doi.org/10.1016/j.epsl.2011.12.036, 2012.

Labrousse, L., Prouteau, G., and Ganzhorn, A. C.: Continental exhumation triggered by partial melting at ultrahigh pressure, Geology, 39, 1171–1174, https://doi.org/10.1130/G32316.1, 2011.

Lang, H. and Gilotti, J.: Partial melting of metapelites at ultrahigh-pressure conditions, Greenland Caledonides, J. Metamorphic Geol., 25, 129–147, https://doi.org/10.1111/j.1525-1314.2006.00687.x, 2007.

Leake, B. E., Woolley, A. R., Arps, C., Birch, W. D., Gilbert, M. C., Grice, J. D., and Youzhi, G.: Nomenclature of amphiboles: report of the subcommittee on amphiboles of the International Mineralogical Association Commission on new minerals and mineral names, Min. Mag., 61, 295–321, https://doi.org/10.1180/minmag.1997.061.405.13, 1997.

Liebscher, A., Franz, G., Frei, D., and Dulski, P.: High-Pressure Melting of Eclogite and the P–T–X History of Tonalitic to Trondhjemitic Zoisite-Pegmatites, Munchberg Massif, Germany, J. Petrol., 48, 1001–1019, https://doi.org/10.1093/petrology/egm008, 2007.

Liu, P. L., Wu, Y., Liu, Q., Zhang, J. F., Zhang, L., and Jin, Z. M.: Partial melting of UHP calc-gneiss from the Dabie Mountains, Lithos, 192–195, 86–101, https://doi.org/10.1016/j.lithos.2014.01.012, 2014.

Liu, P. L., Massonne, H. J., Harlov, D. E., and Jin, Z. M.: High-Pressure Fluid–Rock Interaction and Mass Transfer during Exhumation of Deeply Subducted Rocks: Insights from an Eclogite–Vein System in the Ultrahigh-Pressure Terrane of the Dabie Shan, China, Geochem. Geophys. Geosyst., 20, 5786–5817, https://doi.org/10.1029/2019GC008521, 2019.

Liu, Q., Jin, Z. M., and Zhang, J. F.: An experimental study of dehydration melting of phengite-bearing eclogite at 1.5–3.0 GPa, Sci. Bull., 54, 2090–2100, https://doi.org/10.1007/s11434-009-0140-4, 2009.

Liu, Q., Hermann, J., and Zhang, J. F.: Polyphase inclusions in the Shuanghe UHP eclogites formed by subsolidus transformation and incipient melting during exhumation of deeply subducted crust, Lithos, 177, 91–109, https://doi.org/10.1016/j.lithos.2013.06.010, 2013.

Liu, Y. C., Deng, L. P., and Gu, X. F.: Multistage exhumation and partial melting of high-T ultrahigh-pressure metamorphic rocks in continental subduction-collision zones, Sci. China: Earth Sci., 58, 1084–1099, https://doi.org/10.1007/s11430-015-5067-9, 2015.

Malaspina, N., Hermann, H., Scambelluri, M., and Compagnoni, R.: Multistage metasomatism in ultrahigh-pressure mafic rocks from the North Dabie Complex (China), Lithos, 90, 19–42, https://doi.org/10.1016/j.lithos.2006.01.002, 2006.

Martin, C. and Duchêne, S.: Residual water in hydrous minerals as a kinetic factor for omphacite destabilization into symplectite in the eclogites of Vårdalsneset (WGR, Norway), Lithos, 232, 162–173, https://doi.org/10.1016/j.lithos.2015.06.021, 2015.

Masotta, M., Laumonier, M., and McCammon, C.: Transport of melt and volatiles in magmas inferred from kinetic experiments on the partial melting of granitic rocks, Lithos, 318–319, 434–447, https://doi.org/10.1016/j.lithos.2018.08.032, 2018.

Michaud, J. A. S., Pichavant, M., and Villaros, A.: Rare elements enrichment in crustal peraluminous magmas: insights from partial melting experiments, Contrib. Mineral. Petrol., 176, 96, https://doi.org/10.1007/s00410-021-01855-9, 2021.

Möller, C.: Decompressed eclogites in the Sveconorwegian (–Grenvillian) orogen of SW Sweden: petrology and tectonic implications, J. Metamorphic Geol., 16, 641–656, https://doi.org/10.1111/j.1525-1314.1998.00160.x, 1998.

Moulas, E., Kostopoulos, D., Connolly, J. D., and Burg, J. P.: P-T estimates and timing of the sapphirine-bearing metamorphic overprint in kyanite eclogites from Central Rhodope, northern Greece, Petrology, 21, 507–521, https://doi.org/10.1134/S0869591113050032, 2013.

Moulas, E., Tajčmanová, L., Vrijmoed, C., and Podladchikov, Y.: Mechanically- v. diffusion-controlled metamorphic microstructure: a symplectite example from Rhodope Metamorphic Complex (Greece), J. Metamorphic Geol., 33, 849–858, https://doi.org/10.1111/jmg.12141, 2015.

Nakamura, D. and Hirajima, T.: Granulite-facies overprinting of ultrahigh-pressure metamorphic rocks, northeastern Su–Lu region, eastern China, J. Petrol., 20, 563–582, https://doi.org/10.1093/petrology/41.4.563, 2000.

Obata, M.: Kelyphite and Symplectite: Textural and Mineralogical Diversities and Universality, and a New Dynamic View of Their Structural Formation. In: New Frontiers in Tectonic Research-General Problems, Sedimentary Basins and Island Arcs (Chapter 5), edited by: Sharkov, E. V., 93–122, publisher: In Tech, https://doi.org/10.5772/20265, 2011.

Okay, A. I., Xu, S. T., and Sengor, A. M. C.: Coesite from the Dabie Shan Eclogites, Central China, Eur. J. Mineral., 1, 595–598, https://doi.org/10.1127/ejm/1/4/0595, 1989.

Palin, R. M., White, R. W., and Green, E. C. R.: Partial melting of metabasic rocks and the generation of tonalitic-trondhjemitic-granodioritic (TTG) crust in the archaean: Constraints from phase equilibrium modelling, Precambr. Res., 287, 73–90, https://doi.org/10.1016/j.precamres.2016.11.001, 2016.

Patiño Douce, A. E., and Harris, N.: Experimental Constraints on Himalayan Anatexis, J. Petrol., 39, 689–710, https://doi.org/10.1093/petroj/39.4.689, 1998.

Putnis, A.: Mineral replacement reactions, Rev. Mineral. Geochem., 70, 87–124, https://doi.org/10.2138/rmg.2009.70.3, 2009.

Rodriguez-Navarro, C., Cultrone, G., Sanchez-Navas, A., and Sebastian, E.: TEM study of mullite growth after muscovite breakdown, Am. Mineral., 88, 713–724, https://doi.org/10.2138/am-2003-5-601, 2003.

Rosenberg, C. L. and Handy, M. R.: Experimental deformation of partially melted granite revisited: implications for the continental crust, J. Metamorphic Geol., 23, 19–28, https://doi.org/10.1111/j.1525-1314.2005.00555.x, 2005.

Rushmer, T.: Volume change during partial melting reactions: implications for melt extraction, melt geochemistry and crustal rheology, Tectonophysics, 342, 389–405, https://doi.org/10.1016/S0040-1951(01)00172-X, 2001.

Sawyer, E. W.: Melt segregation in the continental crust: distribution and movement of melt in anatectic rocks, J. Metamorphic Geol., 19, 291–309, https://doi.org/10.1046/j.0263-4929.2000.00312.x, 2001.

Skjerlie, K. P. and Patiño Douce, A, E.: The fluid-absent partial melting of a zoisite-bearing quartz eclogite from 1.0 to

3.2 GPa: implication for melting in thickened continental crust and for subduction-zone processes, J. Petrol., 43, 291–314, https://doi.org/10.1093/petrology/43.2.291, 2002.

Song, S. G., Niu, Y. L., Su, L., Wei, C. J., and Zhang, L.: Adakitic (tonalitic–trondhjemitic) magmas resulting from eclogite decompression and dehydration melting during exhumation in response to continental collision, Geochim. Cosmochim. Acta, 130, 42–62, https://doi.org/10.1016/j.gca.2014.01.008, 2014.

Spicer, E. M., Stevens, G., and Buick, I. S.: The low-pressure partial-melting behaviour of natural boron-bearing metapelites from the Mt. Stafford area, central Australia, Contrib. Mineral. Petrol., 149, 160–179, https://doi.org/10.1007/s00410-004-0577-z, 2004.

Štípská, P., Powell, R., White, R. W., and Baldwin, J. A.: Using calculated chemical potential relationships to account for coronas around kyanite: an example from the Bohemian Massif, J. Metamorphic Geol., 28, 97–116, https://doi.org/10.1111/j.1525-1314.2009.00857.x, 2010.

Stepanov, A. S., Hermann, J., Korsakov, A. V., and Rubatto, D.: Geochemistry of ultrahigh-pressure anatexis: fractionation of elements in the Kokchetav gneisses during melting at diamond-facies conditions, Contrib. Mineral. Petrol., 167, 1002, https://doi.org/10.1007/s00410-014-1002-x, 2014.

Tajčmanová, L., and Konopásek, J.: Diffusion-controlled development of silica-undersaturated domains in felsic granulites of the Bohemian Massif (Variscan belt of Central Europe), Contrib. Mineral. Petrol., 153, 237–250, https://doi.org/10.1007/s00410-006-0143-y, 2007.

Tajčmanová, L., Connolly, J. A. D., and Cesare, B.: A thermodynamic model for titanium and ferric iron solution in biotite, J. Metamorphic Geol., 27, 153–165, https://doi.org/10.1111/j.1525-1314.2009.00812.x, 2009.

Tang, P., Guo, S., Yang, Y. H., Chen, Y., and Su, B.: Evolution of fluids and melts in deeply subducted continental crust: Insights from an UHP eclogite–vein system in the Dabie terrane, China, Lithos, 398–399, 106325, https://doi.org/10.1016/j.lithos.2021.106325, 2021.

Taylor, W. R.: An experimental test of some geothermometer and geobarometer formulations for upper mantle peridotites with application to the thermobarometry of fertile Iherzolite and garnet websterite, Neues Jahrbuch Fur Mineralogie Abhandlungen, 172, 381–408, https://doi.org/10.1127/njma/172/1998/381, 1998.

Tual, L., Pitra, P., and Möller, C.: P–T evolution of Precambrian eclogite in the Sveconorwegian orogen, SW Sweden, J. Metamorphic Geol., 35, 493–515, https://doi.org/10.1111/jmg.12242, 2017.

Tumiati, S., Zanchetta, S., Pellegrino, L., Ferrario, C., Casartelli, S., and Malaspina, N.: Granulite facies overprint in garnet peridotites and kyanite eclogites of monte duria (central alps, italy): clues from srilankite- and sapphirine-bearing symplectites, J. Petrol., 59, 115–151, https://doi.org/10.1093/petrology/egy021, 2018.

Vernon, R. H.: Microstructures of melt-bearing regional metamorphic rocks, Geol. Soc. Am. Mem., 207, 1–11, https://doi.org/10.1130/2011.1207(01), 2011.

Wang, L., Kusky, T. M., Polat, A., Wang, S. J., Jiang, X. F., Zong, K. Q., Wang, J. P., Deng, H., and Fu, J. M.: Partial melting of deeply subducted eclogite from the Sulu orogen in China, Nat. Commun., 5, 5604, https://doi.org/10.1038/ncomms6604, 2014.

Wang, S. J., Wang, L., Brown, M., Piccoli, P., Johnson, T., Feng, P., Deng, H., Kitajima, K., and Huang, Y.: Fluid generation and evolution during exhumation of deeply subducted UHP continental crust: Petrogenesis of composite granite–quartz veins in the Sulu belt, China, J. Metamorphic Geol., 35, 601–629, https://doi.org/10.1111/jmg.12248, 2017.

Wang, S. J., Brown, M., Wang, L., Johnson, T. E., Olierlook, H. K. H., Kirkland, C. L., Kylander-Clark, A., Evans, N. J., and McDonald, B. J.: Two-stage exhumation of deeply subducted continental crust: Insight from zircon, titanite, and apatite petrochronology, Sulu belt of eastern China. GSA Bull., 1/2, 48-66, https://doi.org/10.1130/B36309.1, 2023.

White, R. W. and Powell, R.: On the interpretation of retrograde reaction textures in granulite facies rocks, J. Metamorphic Geol., 29: 131–149, https://doi.org/10.1111/j.1525-1314.2010.00905.x, 2011.

White, R. W., Powell, R., and Holland, T. J. B.: Progress relating to calculation of partial melting equilibria for metapelites, J. Metamorphic Geol., 25, 511–527, https://doi.org/10.1111/j.1525-1314.2007.00711.x, 2007.

Whitney, D. L. and Evans, B. W.: Abbreviations for names of rock-forming minerals, Am. Mineral., 95, 185–187, https://doi.org/10.2138/am.2010.3371, 2010.

Wimmenauer, W. and Stenger, R.: Acid and intermediate HP metamorphic rocks in the Schwarzwald (Federal Republic of Germany), Tectonophysics, 157, 109–116, https://doi.org/10.1016/0040-1951(89)90344-2, 1989.

Xia, Q. X., Zheng, Y. F., and Zhou, L. G.: Dehydration and melting during continental collision: constraints from element and isotope geochemistry of low-T/UHP granitic gneiss in the Dabie orogen, Chem. Geol., 247, 36–65, https://doi.org/10.1016/j.chemgeo.2007.09.013, 2008.

Xu, S. T., Su, W., Liu, Y. C., Jiang, L. L., Ji, S. Y., Okay, A., and Sengör, A. M. C.: Diamond from the Dabie Shan metamorphic rocks and its implication for tectonic setting, Science, 256, 80–82, https://doi.org/10.1126/science.256.5053.80, 1992.

Zeng, L. S., Liang, F. H., Asimow, P., Chen, F. Y. and Chen, J.: Partial melting of deeply subducted continental crust and the formation of quartzofeldspathic polyphase inclusions in the Sulu UHP eclogites, Chinese Sci. Bull., 54, 580–2594, https://doi.org/10.1007/s11434-009-0426-6, 2009.

Zhang, R. Y., Liou, J. G., and Ernst, W.: The Dabie–Sulu continental collision zone: a comprehensive review, Gondwana Res., 16, 1–26, https://doi.org/10.1016/j.gr.2009.03.008, 2009a.

Zhang, G. B., Zhang, L. F., Song, S. G., and Niu, Y. L.: UHP metamorphic evolution and SHRIMP geochronology of a coesite-bearing meta-ophiolitic gabbro in the North Qaidam, NW China, J. Asian Earth Sci., 35, 310–322, https://doi.org/10.1016/j.jseaes.2008.11.013, 2009b.

Zheng, Y. F., Zhou, J. B., Wu, Y. B., and Xie, Z.: Low-grade metamorphic rocks in the Dabie–Sulu orogenic belt: a passive-margin accretionary wedge deformed during continent subduction, Int. Geol. Rev., 47, 851–871, https://doi.org/10.2747/0020-6814.47.8.851, 2005.